Heterogeneous Hydrate Nucleation on Calcite $\{10\bar{1}4\}$ and Kaolinite $\{001\}$ Surfaces: A Molecular Dynamics Simulation Study

Numan Mohammad
Department of Physics and Technology
University of Bergen, Norway

June 2016

A thesis submitted in fulfilment of the requirements for the degree of *Master of Science* in Process Technology.

“Seek knowledge from the cradle to the grave.”

Prophet Muhammad (SAW)

Abstract

Natural gas hydrates are of significant interest due to the great amount of methane that can potentially be utilised as an energy source. These methane resources are trapped in ice-like form, which is a concern since hydrates will dissociate upon contact with water. This type of contact happens worldwide through fracture systems that bring seawater or groundwater into the hydrate layers. The result is the release of methane into the ocean, which adds to the carbon content of the ocean. In some cases, the methane bubbles directly through the water column and into the air. The global temperature increase also leads to decreased thickness of the stability region for these hydrates. These methane leaks are a climate concern, as methane is substantially more aggressive than carbon dioxide as a greenhouse gas. This constant hydrate dissociation can also eventually lead to geomechanical instability and associated catastrophic events. Many of the natural gas hydrate systems are in a dynamic mode of hydrate dissociation and hydrate formation from gas supplied through fracture systems below the hydrate layers. Over geological time scales these systems have entered an almost stationary situation of hydrate dissociation from the top and the new hydrate formation from bottom of the hydrate layers.

Calcite, a natural polymorph of calcium carbonate, and kaolinite, a clay mineral, are important minerals in oil and gas reservoirs and gas hydrate-bearing sediments. Therefore, these minerals can influence the hydrate morphology along with the other necessary (formation) conditions. The main objective of this thesis was to use molecular dynamics simulation to investigate heterogeneous hydrate nucleation in systems that allowed minerals (calcite $\{10\bar{1}4\}$ and kaolinite $\{001\}$ surfaces), water and methane interactions at a constant temperature $(273\ \mathrm{K})$ and pressure $(100\ \mathrm{bar})$. The calculated structures and adsorption profiles of water from the calcite system samplings are in good agreement with experimental and theoretical studies.

The peaks of the primary adsorbed layer of water in the density profiles were found at distances of 2.28 Å, 2.73 Å, and 2.76 Å from the calcite, octahedral, and tetrahedral surfaces, respectively, which are in good agreement with theoretical studies. The hydrogen bonding network between water molecules in the first adsorbed layer was completely distorted as a result of strong calcite-water interactions. Furthermore, kaolinite surfaces disturbed this network to some extent. The surface hydroxyl group, acting as both a proton donor and acceptor, was the dominant feature of the octahedral surface to adsorb water. Hydrogen bonding and density profile analysis at the solid-water interface emphasised the hydrophobic nature of the tetrahedral surface. It was found that methane adsorbed better on the kaolinite surfaces compared to the calcite surface in an aqueous environment. Kaolinite surfaces could provide better hydrate nucleation sites due to good adsorption capability for methane and efficient adsorption sites for water without any significant distortion of the hydrogen bonding network between water molecules.

Acknowledgements

First and foremost, I thank Allah Almighty for giving me the strength, determination and patience to complete this work.

I offer my sincerest gratitude to my supervisor, Professor Bjørn Kvamme, for his valuable input, inspiring guidance and constructive criticism. His knowledge and expertise in the field of gas hydrates and molecular dynamics was very helpful in achieving the goals of the project. His advices, trustworthy support and continuous encouragement was priceless. This accomplishment would not have been possible without his assistance and dedicated involvement in every step throughout research and writing.

I am deeply indebted and grateful to Kim Leirvik who was always willing to help me and give his suggestions. He helped me to learn computer skills and programming in order to overcome hindrances that could otherwise be not possible to be solved out. I would also like to express my gratitude to Richardson Olsen for his insightful comments and suggestions.

Finally, I would like to offer my special thanks to my parents, my brother, and my sisters who were a constant source of support and encouragement for me.

Numan Mohammad

Bergen, June 2016

Contents

List of Figures

List of Tables

Abbreviations

1D	One Dimensional
3D	Three Dimensional
CPU	Central Processing Unit
FMM	Fast Multipole Method
GDIS	GTK Display Interface for Structures
H-bonds	Hydrogen bonds
L-J	Lennard-Jones potential
LAMMPS	Large-scale Atomic/Molecular Massively Parallel Simulator
MD	Molecular Dynamics
P/T	Pressure and Temperature
PBC	periodic boundary conditions
PM	particle-mesh method
PP	particle-particle method
PPPM or P^3M	The Particle-Particle-Particle-Mesh Method
sH	structure H
sI	structure I
sII	structure II
VMD	Visual Molecular Dynamics

1 Introduction

The widespread geographical scattering and huge amount of reserves make gas hydrates a potential energy source [1]. As the oil tipping point has already been breached [2], oil production rates are declining rapidly and will not be able to meet energy demands in the future [3]. Ecological problems are becoming more severe [4] as about 98% of carbon emissions are being released by fossil fuel combustion which is the primary energy source today [5]. Natural gas is the cleanest burning fossil fuel [6], and may act as a 'bridge fuel' in the transition of global energy production from fossil fuels to near-zero carbon emission energy systems [7]. Methane as a potential energy source is available in the form of gas hydrates in marine sediments and permafrost regions [8]. Seismic surveys have identified massive deposits of methane hydrates worldwide [9, 10], but technological challenges [11] and geological hazards [12] prevent exploiting these resources. Gas hydrates are a serious threat to the climate as methane emissions from dissociating hydrates into the atmosphere could lead to global warming [5].

Carbon dioxide, the primary greenhouse gas, is released predominantly from fossil fuel combustion [13] and efforts are being made to reduce its concentration in the atmosphere by sequestering it in deep sedimentary formations [14, 15] and exchanging it with methane in naturally occurring gas hydrates [16, 17]. The fluid flow in geological formations is dependent on both the properties of rocks and fluid [4].The process of gas hydrate formation and deformation in nature relies on a number of factors such as P/T conditions, gas composition, the texture and porosity of sedimentary rocks, and the species residing in that environment [18]. The characteristics and nature of the sedimentary rocks influence the hydrate morphology along with other necessary (formation) conditions, although hydrate morphology can also modify some physical properties of gas hydrate-bearing-sediments [19]. It is crucial to comprehend the formation mechanism and process, the build-up of methane hydrates, and the role of sedimentary rocks on gas hydrate formation and deformation processes in nature.

2 Definition of the Project

Heterogeneous formation of hydrates on the interface between water in pores and gas is the hydrate formation route normally considered. However, it is well known from theoretical studies and experiments that minerals have a substantial structuring effect on water. This leads to extreme maximums in water density but also associated regions of low water density in the adsorbed layers of water on mineral surfaces. Heterogeneous nucleation of hydrates benefits from two-dimensional mass transport. It is therefore of interest to investigate whether the water

structuring can lead to nucleation of hydrates.

Clay minerals, calcite, and quartz were found as the dominant minerals in the sediments of gas hydrates in the ocean drilling programme on Blake Ridge [20]. As calcite and kaolinite are important minerals in oil and gas reservoirs [21, 22] and gas hydrate-bearing sediments [20, 23, 24], the study on these minerals would enhance our knowledge of enhanced oil recovery, carbon dioxide sequestration, and production from gas hydrates.

The surface reactivity of calcite with ground and surface waters influences the chemical behaviour of soils and sediments in geochemical systems [25]. Furthermore, calcite-water interactions are also of significant value in the global carbon cycle [26] and in many industrial applications [27].

3 Purpose of the Project

The objectives of this thesis are the following:

1. To investigate the mineral/water/methane interactions and the possibility of heterogeneous hydrate nucleation on mineral surfaces.
2. To explore the structuring and adsorption patterns of water on mineral surfaces.
3. To analyse the behaviour of supercritical methane in an aqueous environment near mineral surfaces.

4 Methodology

In studies related to adsorption on the surface, experimental techniques, such as use of an X-ray, do not give direct information on thermodynamic properties of the system and normally only provide structural information. Structure and thermodynamics are uniquely related to each other through the relationship between Helmholtz free energy and the structure in the canonical partition function, but the sampled information from the experiments is found through structure factors. Therefore, there is no direct link between thermodynamics and the sample responses from the experiments. Yet, another limitation is the lack of dynamic information. Adsorption involves substantial changes in molecular motions which affects entropy changes as well as the associated heat which needs to be transported away from the adsorption site. These aspects

are very important features of the adsorption dynamics as well as the adsorption stability and characteristics. Experimental methods were therefore not an option for this study.

As the systems under consideration consist of a large number of molecules, *ab initio* simulation cannot be applied. Molecular dynamics and Monte Carlo are the widely used methods for investigating modelling of the atomic-level of fluids. The Monte Carlo method generates configurations of a system using random sampling approach based on positions of atoms to find thermodynamic properties. It lacks a momentum aspect and thus is not appropriate for evaluating time-dependent quantities. The scientific method used in this work is molecular dynamics (MD) which is well suited to study the time evolution of a microscopic system. Molecular dynamics provides a way to attain kinetic and thermodynamic properties based on positions, velocities and orientations of atoms of the system at atomic-level modelling.

5 Natural Gas Hydrates

This section gives a general review of the history, fundamentals, and importance of gas hydrates.

5.1 Historical Development

In 1778, Joseph Priestley was the first person who obtained the hydrate of sulphur dioxide under laboratory conditions. But he could not understand and document this phenomenon. In 1811, Sir Humphery Davy found ice-like material from the saturated aqueous solution of chlorine at temperature below 9 ^{o}C. Davy is considered the first discoverer of hydrate by most of the specialists. Some scientists continued to research it, which was helpful from an academic point of view. The focus was to find which compounds could form hydrates and under what conditions they would form. During the early stages of the natural gas business, gas hydrates were never encountered, as the production and transportation were done at relatively low pressures. As the natural gas business expanded in the twentieth century, high pressure operations progressed for the production, processing, and transportation of natural gas.

The energy balance of the world began shifting towards oil and gas during the early twentieth century. The second phase of gas hydrates started in 1934 when Hammerschmidt [28] concluded that hydrates were troubling gas transportation in the pipelines. Hammerschmidt's research suggested the basic principles of gas hydrate formation in the pipelines as well as some fundamentals to avoid gas hydrate formation. In 1945, Professor Katz published a universal diagram that was helpful in estimating pressure for hydrate formation at a given temperature and gas gravity. The molecular structure of gas hydrates and pressure-temperature conditions for hydrate formation were further investigated during that period.

The third phase of gas hydrates began with the discovery of natural gas hydrates. This discovery highlighted the significance of and promoted the research on gas hydrates. Gas hydrates can exist in nature, which was proved through several experiments in the 1960s. It was necessary to discover and estimate the resources of gas hydrates in order to increase the public and political interests in this field. Surveys were devised to estimate the gas hydrate resources both onshore and offshore. Scientists are still working to estimate the correct amount of resources that could be exploited. The production of natural gas hydrates is a big issue today as gas hydrates are being considered a potential energy source [18, 29–31].

5.2 Gas Hydrate Structures

Gas hydrates are ice-like solid crystalline compounds that form when slightly polar or non-polar guest molecules get trapped inside cages of water molecules. Three crystalline structures of natural gas hydrate has been proposed by Sloan and Koh [32] among them structure I and II are common in the petroleum industry whereas structure H is rarely found, described as follows:

Structure I The guest molecules with diameters between 4.2 Å and 6 Å form sI hydrates with water. Its crystal structure is cubic. A unit cell is made up of 46 water molecules. The unit cell has two small and six large cavities. The small cavity is a pentagonal dodecahedron that is a 12-sided polyhedron with pentagonal faces. The large cage is a Tetrakaidecahedron that is a 14-sided polyhedron with twelve pentagonal faces and two hexagonal faces. The common guest molecules that form sI hydrates are methane, ethane, hydrogen sulphide, and carbon dioxide. Ethane molecules occupy only large cages, while others can occupy both the small and large cages.

Structure II Structure II hydrates are formed when guest molecules have diameters less than 4.2 Å like nitrogen. Guest molecules with a radius between 6 Å and 7 Å also form this cubic structure. A unit cell is made up of 136 water molecules. The unit cell has 16 small and eight large cavities in one unit cell. The small cavity is a pentagonal dodecahedron that is a 12-sided polyhedron with pentagonal faces. The large cage is a hexakaidecahedron which is a 16-sided polyhedron with 12 pentagonal faces and four hexagonal faces. The common guest molecules that form structure II hydrates are propane, isobutane, and nitrogen. Propane and isobutene occupy only the large cages, whereas nitrogen can occupy both.

Structure H Larger guest molecules (7 Å $<$ diameter $<$ 9 Å) such as iso-pentane form structure H when accompanied by smaller molecules such as nitrogen and methane. Hydrates of this type are much less common. A unit cell is made up of 34 water molecules. The unit cell has three small, two medium, and one large cavity. The small cavity is a pentagonal dodecahedron that is a 12-sided polyhedron with pentagonal faces. The medium cavity is an irregular dodecahedron consisting of three square faces, six pentagonal faces, and three hexagonal faces, while the large cage is an irregular icosahedron, a 20-sided polyhedron with 12 pentagonal faces and eight hexagonal faces. Two guest molecules are required to form structure H hydrates. The large molecule occupies only the large cage, while small molecules occupy both the small and medium cages [30, 31].

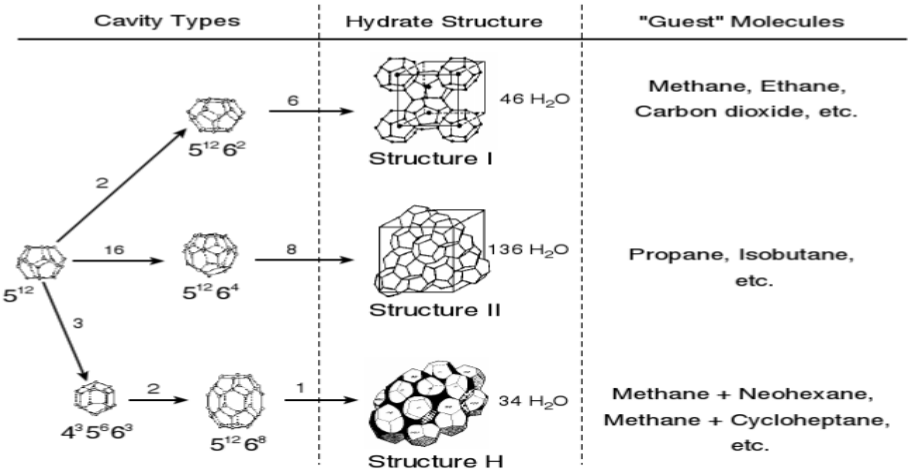

Figure 5.1: Schematic of gas hydrate structures. The left column indicates the number of cavities (above arrow line). Types of cavities are pictured with the number of pentagonal and hexagonal faces (below each picture). The middle column shows the smallest repeating units and number of water molecules necessary to build a unit cell. The right column indicates guest molecules [33].

5.3 The Process of Hydrate Formation

The formation of gas hydrate requires a hydrate former, a sufficient amount of water, and the correct combination of temperature and pressure conditions. Low temperature and high pressure favour this phenomenon, while the composition of the hydrate former decides the right combination temperature and pressure. If any of the three requirements stated are not fulfilled, hydrate formation can be avoided [31].

The hydrate formation process can be categorised as nucleation and growth. Nucleation, the first step in the formation of gas hydrates, is a stochastic process in which small gatherings of water and gas occur and disperse in order to attain critical size. These clusters may either develop or shrink by virtue of variations in density or composition before reaching critical size. Homogeneous nucleation, which is a rare phenomenon in nature, takes place in the absence of impurities whereas heterogeneous nucleation occurs at the interface where surfaces or impurities are likely to be involved. Induction time, also known as lag time, is an important terminology to be acknowledged. It is the time required to form a crystal which can be detected macroscopically. The nucleation step dominates the lag time, but it also involves the onset of growth until the crystal size can be detected macroscopically. When the critical size is achieved, steady growth takes place. The growth of gas hydrates is dependent on the mass transfer of constituents to the crystal surface, heat transfer away from the surface, and kinetics of crystal growth [32].

5.4 Composition of Gas Hydrates

The composition of natural gas hydrates depends on the composition of gas and water and the geological conditions in which hydrates are formed. The volume and type of gases dictate the structure and stability of hydrates. Over geological times, the thermodynamic conditions and gas and water composition vary and can result in the restructuring of existing hydrates. Hydrates containing heavy hydrocarbons indicate the presence of oil reservoirs below the gas hydrate deposits [18]. Gas hydrate deposits can be divided into two forms: primary and secondary [11]. Primary deposits do not melt after formation and usually exist in deep water where rapid change in temperature conditions do not occur over time. Secondary deposits may melt after formation and usually exist in the Arctic onshore [18].

5.5 Importance of Gas Hydrates

Natural gas hydrates are of primary interest for the following reasons [5, 6]:

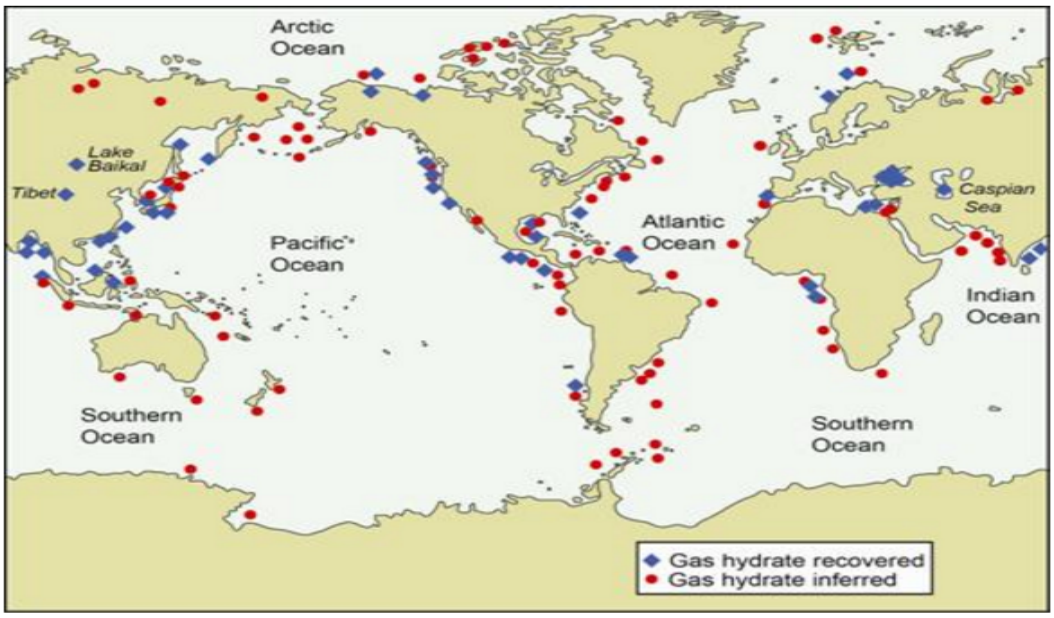

Figure 5.2: Worldwide distribution of gas hydrates (map courtesy: USGS).

1. Natural gas hydrates, enclosing a great amount of methane gas, occur worldwide and may contribute as a new clean energy source.

2. Methane is a greenhouse gas and is more harmful than carbon dioxide. Methane gas from hydrates, if discharged into the atmosphere, would cause global warming.
3. Production of natural gas from hydrates could lead to submarine geohazards.

Gas hydrate resources in nature are estimated to be over 1.5 x 10^{16} m^3 [34]. If we exploit 17% to 20% of this resource, there could be a sufficient supply of energy for 200 years. Gas hydrate deposits that have been found are located both offshore and onshore. Deposits are mainly located offshore, where conditions are suitable for stable hydrates [18].

Gas hydrates resources are distributed worldwide including in countries that are large consumers and importers of energy. Gas hydrates would allow these countries to generate their own energy sources [35].

6 Molecular Dynamics

Molecular dynamics (MD) is a computer simulation technique for studying the time evolution of a system to attain required kinetic and thermodynamic properties by solving equations of motion numerically. Classical mechanics and quantum mechanics are the two main families of MD methods based on the model and mathematical approach chosen for the system. The classical approach considers molecules to be classical objects closely resembling the ball and stick model, whereas quantum mechanics involves the explicit quantum nature of a chemical bond. Computer simulation allows us to model a physical system that is followed by the calculation of physical properties using a mathematical approach [36].

An MD simulation describes the change in positions, velocities and orientations with respect to time at the molecular or atomic level in order to study bulk properties. Initial conditions and interaction forces are the main ingredients to observe the behaviour of a system [37]. An MD simulation generates molecular trajectories (phase space trajectory) for each individual atom that consists of 3N-dimensional configuration space and 3N-dimensional momentum space. The former describes the coordinate axis for position vectors while the latter defines the coordinate axis for momentum vectors. These are computed by solving numerically Newton's second law of motion. The phase space is the 6N dimensional space that represents all the positions and momenta of the atoms or particles in a given system. The points in phase space are updated with time. The relation between force **F** and acceleration **a** is governed by Newton's equation of motion shown as follows:

$$\mathbf{F} = m\frac{d^2\mathbf{r}}{dt^2} = m\mathbf{a} \tag{1}$$

where t is time, **r** the position vector, m the mass of the particle.

Care must be taken while choosing the initial configuration, as it can often dictate the success or failure of a simulation. The disorder in early arrangements of the atoms or molecules could lead to higher energy interactions that may result in instabilities in the system. This can often be avoided by performing energy minimisation of the system before running the simulation [38].

The relation between force exerted on particles of a given system and the potential energy is given as follows:

$$\mathbf{F} = -\nabla U \tag{2}$$

This potential term U consists of intermolecular and intramolecular interactions of particles in the system. It can be written as:

$$U = U_{bonded} + U_{non-bonded} \tag{3}$$

U_{bonded} represents intramolecular contributions as follows:

$$U_{bonded} = U_{bondstretching} + U_{anglebending} + U_{torsionterms} \tag{4}$$

$U_{nonbonded}$ represents intermolecular contributions that introduce the attraction and repulsion terms between molecules.

$$U_{nonbonded} = U_{electrostatics} + U_{vdw} \tag{5}$$

This section gives a general overview of MD simulation, emphasising the topics related to this thesis.

6.1 The Ensemble

An ensemble is defined by a set of systems that are macroscopically identical while having different microscopic states. A microscopic state represents the position and momentum of each particle in the system. The microscopic states of a system consisting of N atoms at a given time are represented by $(\mathbf{r}_1, \mathbf{r}_2, \mathbf{r}_3 \ldots . \mathbf{r}_N, \mathbf{p}_1, \mathbf{p}_2, \mathbf{p}_3 \ldots . \mathbf{p}_N)$.

It is not possible to compute equation of motions for N particles where N can be any number of particles (e.g., 10^{23}) in a real system. The macroscopic properties of the large systems usually show orderly behaviour and are independent of individual behaviour of the particles, thus rarely showing significant deviations. A few variables are controlled in a system to evaluate the time evolution of the positions and momenta of the particles that further help to obtain macroscopic properties of the real system under specified constraints [40]. Statistical mechanics uses probability theory providing a way to link microscopic dynamics with macroscopic thermodynamics [39]. It estimates the macroscopic properties of the materials from the interactions of atoms and molecules at the microscopic level. Therefore, the systems of atoms and molecules are used to study the real systems (or materials) that are useful in everyday life in order to study the thermodynamic properties of the systems.

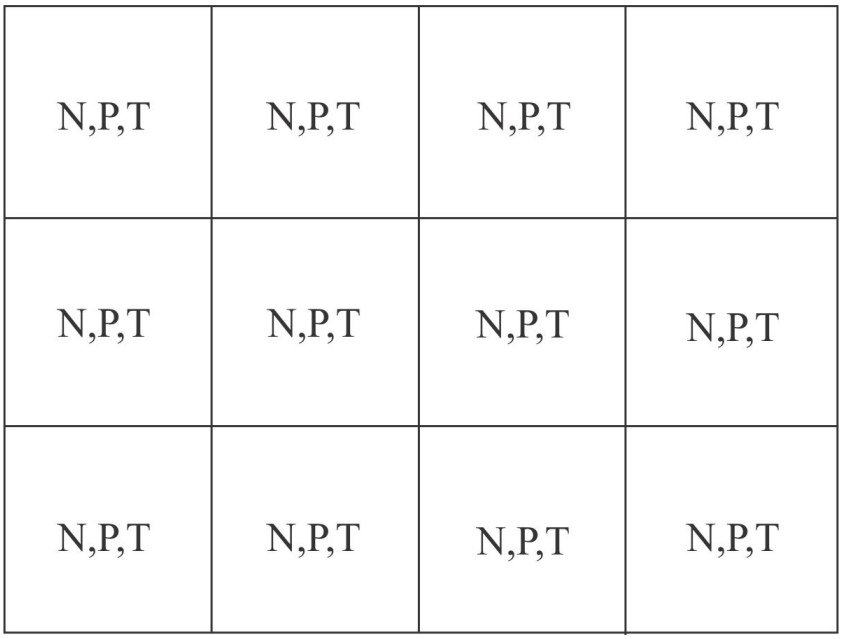

Figure 6.1: NPT ensemble. The number of particles N, the temperature T, and the pressure P are the variables that are fixed in each cell.

The atomic approach to study the macroscopic behaviour was first suggested by Maxwell who studied the distribution law of molecular velocities, followed by Boltzmann who introduced the related equations [40].

Depending on the variables that we control, three ensemble approaches are usually used to define a system, and each has its own features given as follows:

Micro-canonical Ensemble: It represents an isolated system. The number of particles N, the total energy E, and the volume V are the variables that are fixed in each cell.

Canonical Ensemble: A system is in contact with a heat bath. The number of particles N, the volume V, and the temperature T are the variables that are fixed, while energy can fluctuate.

Grand canonical ensemble: This system is in contact with heat and particle bath. The volume V, the temperature T, and the chemical potential are the variables that are fixed, while the number of particles can fluctuate [44].

Now consider a system which is surrounded by a heat bath that keeps the temperature of the system constant. A collection of replicas of this system makes canonical ensemble, each cell having constant volume. As there is no restriction to the flow of energy between the system and the heat bath, energy of the replicas can differ. Let us suppose, total energies of N particles

contained in each cell are represented by $E_1, E_2, E_3 \ldots . E_N$, the canonical partition function is given as:

$$Q = \sum_i exp\Big(- \frac{E_i}{k_B T} \Big) \tag{6}$$

Canonical partition function is used to calculate thermodynamic properties in a canonical ensemble as follows:

$$U = \frac{k_B T^2}{Q} \Big(\frac{\partial Q}{\partial T} \Big)_V \tag{7}$$

$$A = -k_B T ln Q \tag{8}$$

$$H = U + pV \tag{9}$$

$$S = k_B ln Q + k_B T \Big((\frac{\partial Q}{\partial T})_{N,V} \Big) \tag{10}$$

$$G = H - TS \tag{11}$$

where U is average internal energy, A Helmholtz free energy, H enthalpy, S entropy and G Gibbs free energy.

When all the points in phase space that contributed to the total energy are considered in partition function, the expression for canonical partition function becomes:

$$Q = \frac{1}{N!} \frac{1}{h^{3N}} \int \int exp\Big(- \frac{E}{k_B T} \Big) d\mathbf{p} d\mathbf{q} \tag{12}$$

E is often replaced by Hamiltonian H which is the sum of potential and kinetic energy [44].

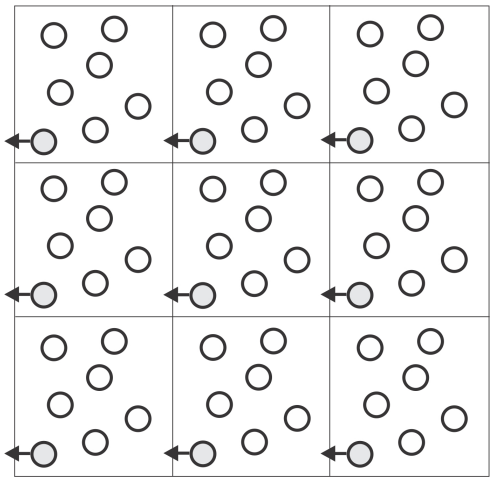

Figure 6.2: Periodic boundary conditions (shown only in one direction).

6.2 Boundary Conditions

Boundary conditions play an important role in solving numerical integration, and dictate the particular solution that we require from the given governing equations [41]. Simulations, containing a relatively small number of particles, are prepared to calculate macroscopic properties so the correct choice of constraints is vital for simulation techniques [38].

It is not possible to study a system containing large number of molecules, as this requires infinite time to compute the forces and trajectories of a system. Periodic boundary conditions (PBC) provides a way to analyse a small number of molecules and can facilitate implementing these results in a large system. A system containing a small number of molecules with a finite volume V is called a primary cell. It represents a small portion of the bulk material that is surrounded by the exact replicas of the primary cell. Each image cell has the same size and shape and contains the same number of particles as the primary cell [37].

Surface effects are usually eliminated, as there are very few atoms that actually interact with the wall in the real system. The PBC are usually used to study the properties and behaviour of bulk fluid but not its interaction with the wall. The number of particles remains constant in the primary cell because if any particle leaves the primary cell during simulation, it will re-appear on the other side of the box as shown in Figure 6.2. However, it is not hard and fast rule to use PBC in all directions in molecular dynamics simulation [38].

6.3 The Verlet Algorithm

There are various integration methods used in MD. The Verlet algorithm is among the most widely used in simulation [37]. Verlet's simplicity and stability [36] make it an easier choice.

$$\mathbf{r}_i(t+\Delta t) = \mathbf{r}_i(t) + (\frac{d\mathbf{r}_i}{dt})_t\Delta t + \frac{1}{2}(\frac{d^2\mathbf{r}_i}{dt^2})_t(\Delta t)^2 + ... \tag{13}$$

$$\mathbf{r}_i(t-\Delta t) = \mathbf{r}_i(t) - (\frac{d\mathbf{r}_i}{dt})_t\Delta t + \frac{1}{2}(\frac{d^2\mathbf{r}_i}{dt^2})_t(\Delta t)^2 + ... \tag{14}$$

$$\mathbf{r}_i(t+\Delta t) = 2\mathbf{r}_i(t) - \mathbf{r}_i(t-\Delta t) + (\frac{d^2\mathbf{r}_i}{dt^2})_t(\Delta t)^2 \tag{15}$$

$$\mathbf{v}_i(t) = \frac{\mathbf{r}_i(t+\Delta t) - \mathbf{r}_i(t-\Delta t)}{2\Delta t} \tag{16}$$

These equations describe the basic Verlet algorithm approach.

The basic Verlet and leap-frog schemes do not compute positions and velocities at the same instant of time; therefore, kinetic and potential energies are defined at different times. To overcome this inconvenience, there is another form of the Verlet algorithm called the velocity Verlet algorithm. In this algorithm, the position and velocity are computed at the same value of time [42]. The standard velocity Verlet integrator is given as follows [44]:

$$\mathbf{r}_i(t+\Delta t) = \mathbf{r}_i(t) + (\frac{d\mathbf{r}_i}{dt})_t\Delta t + \frac{1}{2}(\frac{d^2\mathbf{r}_i}{dt^2})_t(\Delta t)^2 \tag{17}$$

$$\mathbf{v}_i(t+\Delta t) = (\frac{d\mathbf{r}_i}{dt})_t + \frac{1}{2}((\frac{d^2\mathbf{r}_i}{dt^2})_t + (\frac{d^2\mathbf{r}_i}{dt^2})_{t+\Delta t})\Delta t \tag{18}$$

6.4 Intramolecular Terms

Intramolecular terms are the bonded interactions between the atoms within a molecule. These interactions are influenced by the molecule itself and by the atoms of the neighbouring molecules.

6.4.1 Bond Stretching

The ball and spring model is commonly used to describe a covalent bond in a molecule where atoms are treated as balls that interact through the covalent bond represented by a spring.

The simplest approach to describe bond stretching is Hooke's law, which relates the restoring force with the square root of the displacement from the reference bond length [38].

$$F = -k(r - r_e) \tag{19}$$

where

F is the restoring force of the spring

k is the force constant of the spring

r_e represents equilibrium length of the spring, and

$r - r_e$ is the spring displacement from its equilibrium position.

The negative sign indicates that the force is opposing the direction of displacement. It means that the bond tries to restore its equilibrium position. Bond stretching contributes to the potential energy that is given as:

$$U_{bondstretching} = \frac{k_{str}}{2}(r - r_e)^2 \tag{20}$$

where k_{str} is the force constant, and r_e is the equilibrium bond length while r is the instantaneous bond length. Hooke's law requires two parameters to be specified.

The Morse potential, another approach, is efficient to calculate potential energy of bond stretching over a wide range and is given as follows:

$$U_{bondstretching} = D[1 - exp{-}\alpha(r - r_e)] \tag{21}$$

Each bond requires three parameters to be defined in the Morse potential [38]. Thus it is an expensive way to calculate bond stretching.

6.4.2 Angle Bending

An angle is defined by any three atoms linked by covalent bonds within a molecule. Any fluctuation in an angle that is represented by a spring, results in angle bending potential as the

spring tries to restore its equilibrium position. Angle bending is described by the harmonic potential, similar to bond stretching. The potential energy is given as:

$$U_{anglebending} = \frac{k_{ang}}{2}(\theta - \theta_e)^2 \tag{22}$$

where $\theta - \theta_e$ is the angle deviation from its equilibrium angle.

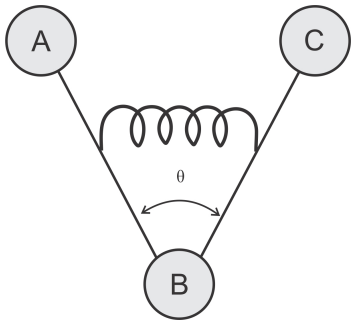

Figure 6.3: Harmonic angle bending.

6.4.3 Torsion Terms

When four or more atoms are bonded together, as shown in Figure 6.4, the torque applied by the bonds A—B and C—D (acting like arms in this case) will result in torsion force around bond B—C. Torsion energy is associated with the rotation about the bonds. It requires a significant amount of energy to introduce notable deformations in a bond or angle from their equilibrium positions, therefore torsion terms and non-bonded interactions play the main role in structural changes and relative energies [38].

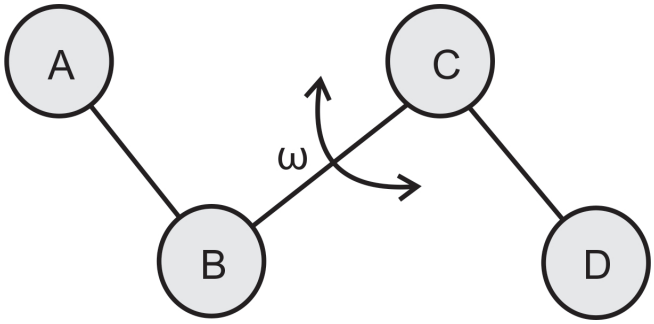

Figure 6.4: Torsion bending.

Torsional energy fundamentally differs from stretch and bending energy in three ways [43]:

1. The torsional energy and non-bonded (electrostatic and Van der Waals) interactions contribute to the rotational barrier. The torsional terms are therefore linked to the non-bonded parameters.
2. The torsion energy function must be periodic; thus, the energy should have the same value if the bond is rotated through an angle of 360°.
3. Large deviations from the minimum energy structure may arise as the energy required to rotate about a bond is generally low. Taylor expansion is therefore not helpful in such situations.

The Fourier series is usually used to model torsional terms:

$$U_{tors}(\omega) = \sum_{n=1} V_n cos(n\omega) \tag{23}$$

The term n=1 represents a rotation that is periodic by 360°, n=2 is periodic by 180°, n=3 is periodic by 120°, and so on. The constants V_n represent the magnitude of rotation barrier around the bond. Some of V_n constants may have zero magnitude depending on the situations.

The force field MM2 uses the following expression for torsional energy [38]:

$$U_{tors}(\omega) = \frac{V_1}{2}(1 + cos\omega) + \frac{V_2}{2}(1 - cos2\omega) + \frac{V_3}{2}(1 + cos3\omega) \tag{24}$$

6.5 Intermolecular Terms

Intermolecular terms are non-bonded interactions between atoms that are not connected through chemical bonds of the same molecule and the atoms of the neighbouring molecules. In a force field, these terms usually consider electrostatic and van der Waals interactions [38]. The most time consuming part of the MD simulation is computing the non-bonded terms.

6.5.1 Electrostatic Interactions

Atoms and molecules are generally electrostatically neutral, as the number of electrons and protons are exactly equal. Whenever there is difference in electronegativity between two or more atoms bonded in a molecule, electrons (involved in bonding) slightly shift towards more electronegative atoms, which distributes the charge within a molecule [44]. Partial charges

result in electrostatic interactions between two molecules (or more precisely the atoms of two molecules), which is calculated using Coulomb's law.

If we represent two point charges by Q_A and Q_B then Coulomb's law states that the electrical force exerted by Q_A on Q_B is directly proportional to the product of the quantity of charges and is inversely proportional to the square of the distance (R) between the two point charges.

$$F = k\frac{Q_A Q_B}{R^2} \tag{25}$$

where k is Coulomb's constant.

The force exerted by Q_B on Q_A is equal to the force exerted by Q_A on Q_B but is opposite in the direction; thus, it satisfies Newton's third law of motion. The electrostatic terms do not decay rapidly with distance and long-range electrostatic interactions are often important to consider in most of the systems.

The potential energy due to the electrostatic contributions is calculated as a sum of pairwise interactions between atoms in the system [38].

$$U_{elec} = \sum_i \sum_j \frac{Q_A Q_B}{4\pi\epsilon_o r_{ij}} \tag{26}$$

where ϵ_o is permittivity of free space.

6.5.2 Van der Waals Interactions

Electrostatic interactions do not include all the non-bonded interactions. Van der Waals interactions involves the interactions (that are not electrostatic) between atoms that are not directly bonded. These interactions between two atoms are very repulsive at short distances and slightly attractive at an intermediate distance, diminishing to zero at long distances. When the electronic cloud between two atoms overlap, it causes strong repulsion. The attraction is mainly dominated by the induced dipole-dipole interactions.

A molecule having no permanent dipole can induce a dipole because of the motion of electrons that will cause a slight uneven distribution of electronic charge at any given time. This dipole will cause a charge polarisation in the neighbouring molecule, creating an attraction that decays at the inverse sixth power of the distance between two atoms.

6.5.3 Lennard-Jones potential

Van der Waals terms are usually modelled using the Lennard-Jones (L-J) potential.

The L-J is defined as:

$$U_{L-J}(r) = 4\epsilon\left[\left(\frac{\sigma}{r}\right)^{12} - \left(\frac{\sigma}{r}\right)^{6}\right] \tag{27}$$

Here r is the separation or distance between two atoms, ϵ represents potential well depth and σ is the collision diameter at which the potential energy is zero. If r_m is the distance between atoms at which the potential energy has the minimum value, we can also express L-J in another form as shown in equation:

$$U_{L-J}(r) = 4\epsilon\left[\left(\frac{r_m}{r}\right)^{12} - 2\left(\frac{r_m}{r}\right)^{6}\right] \tag{28}$$

or

$$U_{L-J}(r) = \left[\left(\frac{A}{r}\right)^{12} - \left(\frac{C}{r}\right)^{6}\right] \tag{29}$$

$$A = 4\epsilon(\sigma^{12}) \quad C = 4\epsilon(\sigma^{6}) \tag{30}$$

L-J potential requires two adjustable parameters to be defined, and is commonly used because of its simplicity. The Buckingham potential is a more accurate model to describe the van der Waals interactions, but it has some drawbacks For example, three adjustable parameters are required to define the potential, and the potential becomes strongly attractive at very small distances [38].

In order to calculate the L-J interaction energy in a polyatomic system, mixing rules are used. The Lorentz-Berthelot mixing rule is commonly applied to compute the L-J parameters in which the collision diameter is given by the arithmetic mean, while the well depth is represented by the geometric mean of the values for pure species:

$$\sigma_{ij} = \frac{1}{2}(\sigma_{ii} + \sigma_{jj}) \tag{31}$$

$$\epsilon_{ij} = \sqrt{\epsilon_{ii}\epsilon_{jj}} \tag{32}$$

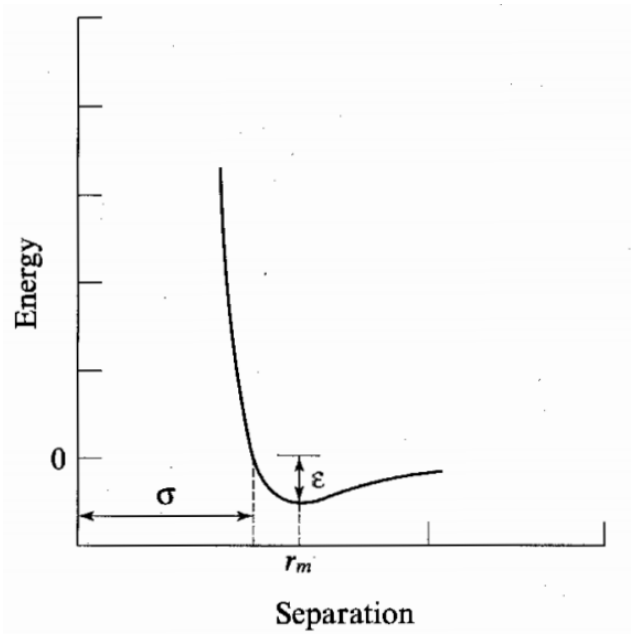

Figure 6.5: Lennard-Jones potential [38].

where ϵ_{ij} is the well depth and σ_{ij} is the collision diameter for interaction between species i and j. Collision diameter is also calculated by geometric mean of the values for pure species in some force fields.

$$\sigma_{ij} = \sqrt{\sigma_{ii}\sigma_{jj}} \tag{33}$$

6.6 Cutoffs

Non-bonded terms are computationally intensive, taking most of the time in MD simulations. If we want to calculate all pairwise contributions in a given system consisting of N particles, it will take infinite time and storage. It is not possible to calculate all the pairwise interactions in the system and thus a cut-off distance for non-bonded interactions is introduced. Non-bonded interactions decrease as the distance increases but care must be taken while choosing the cut-off distance since some long-range interactions can be of significant importance for our system [44].

6.7 Calculation of Long-range Interactions

It is not possible to avoid computationally expensive long-range interactions (e.g., Coulombic interaction) in systems, as truncating the potential contribution by long-range interactions leads to serious inaccuracies. To overcome truncation error and handle long range contributions in a reasonable way, various schemes are used [42]. Ewald, fast multipole method (FMM), and particle-particle-particle-mesh (P^3M) are the three common methods that are used to compute the interactions in a system of N-body particles. The FMM is slower and difficult to implement, while the Ewald method is easier to implement, but may be a better choice for small systems. The P^3M is a fast computational method and is probably the best choice for large systems today. It is more efficient and easier to implement for large systems [45].

6.8 The Particle-Particle-Particle-Mesh Method

The PPPM (or P^3M) is the combination of features of the particle-particle (PP) and particle-mesh (PM) methods. In the PP method, the initial positions and velocities of the particles in a physical system are defined. Then, these values are updated at each time step by evaluating the forces of interactions, and solving equations of motion. It is the simplest and most straightforward approach. In the PM method, a system of particles is interpolated onto a grid and Poisson's equation is solved on the mesh. The potentials and force fields are poorly represented for the particles that are less distant than the mesh spacing. A larger number of mesh points requires more time for the central processing unit (CPU) to attain solution. This limits the resolution of the mesh. The PM method is much faster but is less accurate for close encounters of the particles, while the PP method is slower but more accurate for close encounters of the particles.

The P^3M method is introduced to overcome the limitations of the PP and PM methods. The PP method calculates the total short-range forces on each particle, while the PM method computes the total of the slowly varying forces. These forces are added to obtain the resulting forces on each particle that contribute to updating the velocities. Therefore, the P^3M results in a more accurate and fast computational approach by combining the features of the PP and PM methods [46].

6.9 Thermostats and Barostats

Several methods have been proposed for conducting MD at a constant temperature. Velocity rescaling is the simplest approach to adjust and control the temperature of a given system [44]

as temperature is a measure of instantaneous kinetic energy in a system which is directly related to the velocity of the system. A system consisting of N particles with 3N degrees of freedom and temperature T(t) at time t is denoted as [44]:

$$\left\langle E_{kin} \right\rangle = \left\langle \sum_{i=1}^{N} \frac{1}{2} m_i v_i^2 \right\rangle = \frac{3}{2} N K_B T(t) \tag{34}$$

The velocities are rescaled by a factor of

$$\left(\frac{T_{ref}}{T(t)} \right)^{\frac{1}{2}} \tag{35}$$

where T_{ref} is the reference or desired temperature Velocities of the particles at each time step are scaled to maintain the temperature of the system in this method.

6.9.1 Nose-Hoover Thermostat

An alternative method was suggested by Nose [47] and subsequently improved by Hoover [48]. A system is surrounded by a heat bath (or thermal reservoir) that keeps the temperature of the system constant. This bath is an integral part of the system as energy flows between the system and the heat bath but not the particles. Nose introduced a time scale variable s, its conjugate momentum ps, and a parameter Q in order to extend the Hamiltonian model.

The extended Hamiltonian model proposed by Nose is given by:

$$H_{Nose} = \sum_i \frac{\mathbf{p}_i}{2 m_i s^2} + \phi(\mathbf{q}) + \frac{p_s^2}{2Q} + g K_B t \; ln \; s \tag{36}$$

Here T is the externally set temperature, g the number of degrees of freedom of the physical system, and Q a parameter that represents the behaviour as a mass for the motion of s. The term Q influences the temperature fluctuations as its magnitude governs the coupling between the reservoir and the real system [38].

He associated the potential energy gk_BTlns with the variable s to ensure the recovery of canonical ensemble averages, while the kinetic energy term $Qs/2$ was introduced to construct a dynamic equation for s [49].

Nose introduced the virtual variables to control the temperature. He scaled the time step as $dt' = dt/s$ to obtain the dynamic quantities where dt' is the real time step and dt is the virtual

time step so the length of each time step dt' is unequal [49]. Sampling the system at virtual times leads to uneven results in a real system. It is impractical to investigate the dynamic properties of the system with this uneven sampling. Hoover eliminated the time scaling factor and suggested a new variable (ξ)to simplify the Nose equations of motion.

The Nose-Hoover equations of motion are as follows [48]:

$$\frac{d\mathbf{q}_i}{dt} = \frac{\mathbf{p}_i}{m_i} \tag{37}$$

$$\frac{d\mathbf{p}_i}{dt} = F(\mathbf{q}_i) - \xi \mathbf{p}_i \tag{38}$$

$$\frac{d\xi}{dt} = \frac{[\sum_i \frac{\mathbf{p}_i^2}{m_i} - X k_B T]}{Q} \tag{39}$$

where ξ is thermodynamic friction coefficient.

Nose-Hoover equations, similar to the Nose equations, may result in temperature oscillation so care must be taken while choosing the values of the fictitious mass Q and the extended-system energy. If Q is too large (loose coupling), it may lead to poor temperature control and long simulation times will be needed to obtain canonical distribution. If Q is too small (tight coupling), it may lead to high frequency temperature fluctuations [50].

6.9.2 Nose-Hoover Barostat

Andersen [51] suggested the barostat method to study the dynamics of a system consisting of small number of molecules at constant temperature and pressure conditions. As only volume changes in the Andersen method but not shape, Parrinello et al. [52] extended this method to overcome this limitation for crystal structures [53]. Nose further developed it, and it was later modified by Hoover [48]. It is recommended to follow Hoover [48] to get further information related to equations of motion used in isothermal-isobaric ensembles.

6.10 Constraint Dynamics

The presence of flexible molecules introduces intramolecular interactions influencing the relative orientations of the atoms. In simple models intramolecular interactions are usually ignored and

the dynamics of each molecule are calculated using translational and rotational motion about the centre of mass. But atomic Cartesian coordinates are important to describe conformation of flexible molecules. As we know it requires a significant amount of energy to introduce notable deformations in bonds or angles (high frequency motion) from their equilibrium positions so torsion terms and non-bonded interactions play the main role in structural changes and relative energies. However, ignoring the highest frequency motion in the presence of flexible molecules could lead to inaccuracy in simulation and smaller time steps as the highest frequency motion dictate the time step of the simulation. Constraint dynamics are introduced to increase the time step and the accuracy. This does not affect the other internal degrees of freedom but specifies individual or a combination of internal coordinates [38]. Constraints are often divided into two categories: holonomic or non-holonomic. Holonomic constraints satisfy the following condition [38]:

$$f(q_1, q_2, q_3...., t) = 0 \tag{40}$$

where q_1,q_2,q_3,... represents coordinates of the particles.

The SHAKE algorithm [54] is commonly used for imposing internal constraints in MD. Bonds and/or angles are forced to reset their equilibrium positions at each time step following holonomic constraint [38].

6.11 The H-Bonds Plugin

This plugin is useful in obtaining the number of hydrogen bonds (H-bonds) formed throughout a trajectory. The two atoms are picked to calculate the number of H-bonds formed during a simulation run. One of the atoms can be selected as a donor, an acceptor or both. It plots the number of H-bonds formed over time. The H-bonds plugin defines H-bond by taking into account three arguments:

1. The presence of a hydrogen donor and a hydrogen acceptor.
2. The hydrogen donor and acceptor should be at a given cut-off distance.
3. The angle (D—H. . . .A) must be within the given cut-off angle.

Table 6.1: Properties of the strength of hydrogen bonds [55].

Bond strength	Very strong	Strong	Weak
Bond energy (-kcal/mol)	15-40	4-15	<4
D—A distance	2.2-2.5	2.5-3.2	3.0-4.0
H—A distance	1.2-1.5	1.5-2.2	2.0-3.0
Covalency	Pronounce	Weak	Vanishing

6.11.1 Hydrogen bonding

Hydrogen bonding is a weak interaction relative to a covalent bond but a strong interaction compared to the van der Waals interaction. The H-bond may be defined as any cohesive interaction formed between a proton acceptor and hydrogen atom bonded to an electronegative atom (one or both should be electronegative) like D—H. . . .A wherein D acts as a proton donor and A acts as a proton acceptor. Hydrogen bonding can be categorised as a very strong, strong, or weak interaction, which is described in detail in Table 6.1.

Very strong H-bonds form between unusually activated donors and acceptors (e.g., $[F....H....F]^-$). These forces participate in deciding crystal packing. Strong H-bonds have the ability to hold crystal and supramolecular structure efficiently (e.g., O—H...O—H). These interactions are much stronger compared to the van der Waals forces of attractions. Weak hydrogen bonds form when one or both of the acceptors or donors are weak (e.g., C—H. . . .N) [55].

6.12 Density Profile Tool

This plugin computes one-dimensional density profiles in the Visual Molecular Dynamics (VMD) programme. It helps in understanding the distribution of a particular type of atom or molecule in the primary cell. The density profile can be plotted based on number, mass, electrons, or charge depending on one's choice and requirements. It can be calculated at a particular frame or by averaging the density over the number of frames. An atom or molecule can be selected to analyse its density in one particular direction. Suppose density profile along z-direction is required, the space is divided into equally spaced slabs of thickness Δz. If the indexing of slabs is represented by integer b then spatial region that is denoted by bin b will be $b\Delta z \leq z < (b+1)\Delta z$. The indicator function for slab b is given as:

$$\delta_b = \begin{cases} 1 & \text{if } b \leq \frac{z}{\Delta z} < b+1 \\ 0 & \text{otherwise} \end{cases}$$

The density value at bin b attained by binning the selected atomic property p_i e.g. mass is normalized by the following expression.

$$\rho_b = (L_x L_y z)^{-1} \sum_{i \in atoms} \delta_b(z_i) p_i \tag{41}$$

where $L_x L_y z$ is the volume of slab b, z the z-coordinate of the centre of atom i [56].

7 Literature Survey

This section provides an overview of the previous studies on hydrate formation and deformation conditions in the presence of mineral rocks and the structuring of water and methane on calcite and kaolinite surfaces. First, experimental studies on the role of sedimentary minerals in gas hydrates formation and the dissociation conditions and adsorption patterns of water and methane on these minerals are described. Second, computer simulation research on the ordering of water and interactions at the mineral surface and water interface is discussed. A few of the published research papers are described in detail.

7.1 Experimental Investigations

In Section 7.1.1, the main findings from a study by Chuvilin et al. [57] have been summarised. They performed experiments in a special pressure chamber (as described below) to study factors affecting hydrate formation and deformation in methane-saturated sediments. In Section 7.1.2, X-ray surface scattering experiments, which were used to determine 3D structuring at calcite-water interface, are discussed, as reported by Geissbuhler et al. [58]. Section 7.1.3 illustrates important results related to methane adsorption in clay minerals [59, 60].

7.1.1 Gas hydrate formation/deformation in methane-saturated sediments

A special pressure chamber in which pressure was controlled by a gas cylinder (methane 99.98%), was connected with a computer where temperature and pressure could be recorded. They used a layer-by-layer consolidation technique to prepare samples for analysis. Two samples with the same composition were tested in each experiment: one in the experiment chamber and one outside the chamber at the same temperature conditions. Each cycle of hydrate and ice formation and deformation followed the following steps:

1. The pressure chamber was prepared for analysis. Later, samples were introduced into the chamber. The pressure was raised to 8-9 MPa, exposing the soil samples to methane.
2. The temperature was reduced to +0.5 ^{o}C to 4 ^{o}C by placing the chamber and control sample into a refrigerator.
3. The pressure of the chamber and control sample got stabilised. The primary hydrate formation took place.
4. The temperature was further reduced to -7 ^{o}C to -9 ^{o}C to freezing.

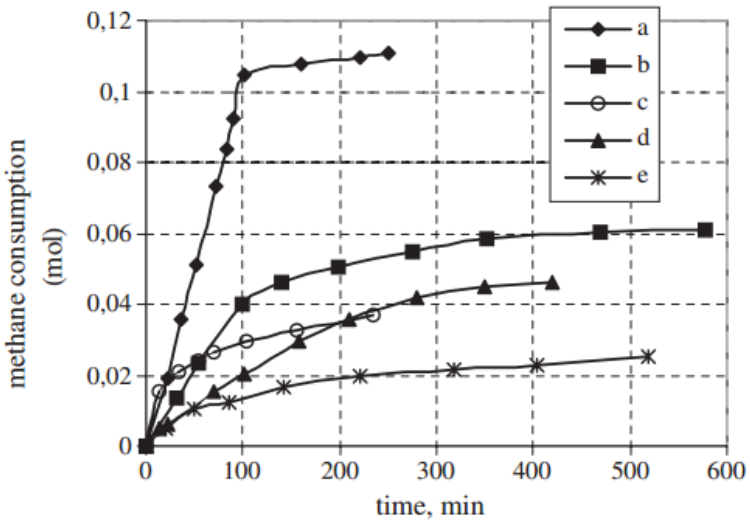

Figure 7.1: The rate of methane consumption for hydrate formation in methane-bearing sediments a: sand (water content: 17%); b: sand with 7% of montmorillonite clay (water content: 17%); c: montmorillonite clay (water content: 70%); d: kaolinite clay (water content: 35%); e: kaolinite clay (water content: 35%, salinity: 0.2%) [57].

5. Temperature was increased gradually to 17 °C to 19 °C to observe hydrate deformation and ice melting.

The experiments were performed on sediments having different water content, porosity, salinity, and composition in order to analyse the factors affecting methane hydrates under various pressure and temperature conditions. It was deduced that the presence of rock minerals influenced the temperature and pressure conditions for hydrate formation and deformation by a number of factors, like the availability of water, salinity, grain size, and mineral composition. The water content used for the kaolinite clay experiment was 35%. Figure 7.1 illustrates the effect of different clay minerals on rate of hydrate formation in which kaolinite clay showed the minimum rate of methane absorption for hydrate formation. The increase in concentration of dissolved salts in kaolinite clay moved the P/T conditions for hydrate deformation to a higher pressure and lower temperature, as described in Figure 7.2 [57].

Uchida et al. [61] investigated the decomposition conditions of methane hydrates in minerals of hydrate-bearing sediments and concluded that the pore size was the dominant factor influencing decomposition conditions [61].

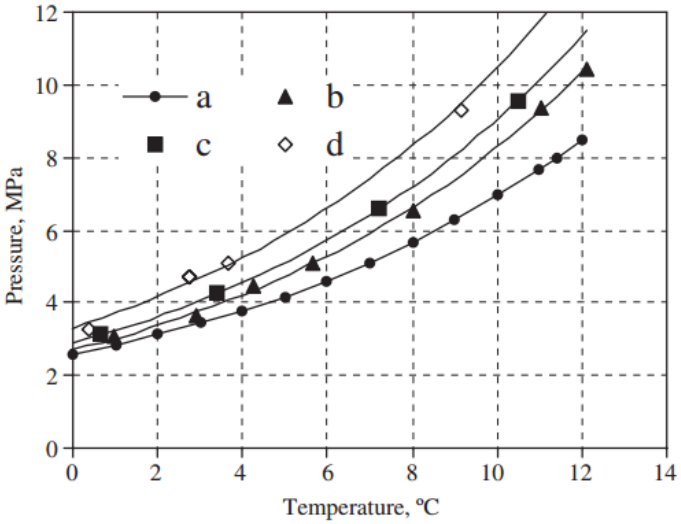

Figure 7.2: P/T conditions of methane hydrate deformation in kaolinite clay a: only gas-water; b: kaolinite clay (salinity: 0 %); c: kaolinite clay (salinity: 0.2%); d: kaolinite clay (salinity: 2%) [57].

7.1.2 Structuring of water on a calcite surface

The X-ray scattering technique was employed to view the 3D structure of the calcite-water interface in which the structuring of hydration layers on the calcite surface was the main focus. They performed repeated measurements to make sure that the X-ray beam did not induce any changes in the calcite-water interface structure.

As two water molecules could occupy each calcite surface unit mesh, they distinguished them by designating them as Ow1 and Ow2 where the initial positions of Ow1 was assumed to be on the calcium ion, while Ow2 was assumed to be on the carbonate ion. Two water sublattices, each beginning with either Ow1 or Ow2, were introduced using atomistic formalism. The two water molecules, Ow1 and Ow2 were allowed to move laterally and vertically while the rigidly connected associated sublattices obeyed the movement of these molecules. The layer spacing was fixed at 2.96Å. They found mild distortions of calcium (Ca) and carbonate (CO_3) ions from their ideal bulk positions in the outermost layer in which displacement in positions of Ca and CO_3 groups, and small rotations of CO_3 groups was observed. It also influenced the second layer. If only one water molecule was allowed to adsorb on the calcite surface, it affected the quality of the experimental results. Therefore, the relaxation of the first two calcite surface layers and a hydration layer containing two inequivalent water molecules were the pre-requisites.

They found the heights of the water molecules Ow1 and Ow2 at a distance of 2.3$\pm$0.1 and

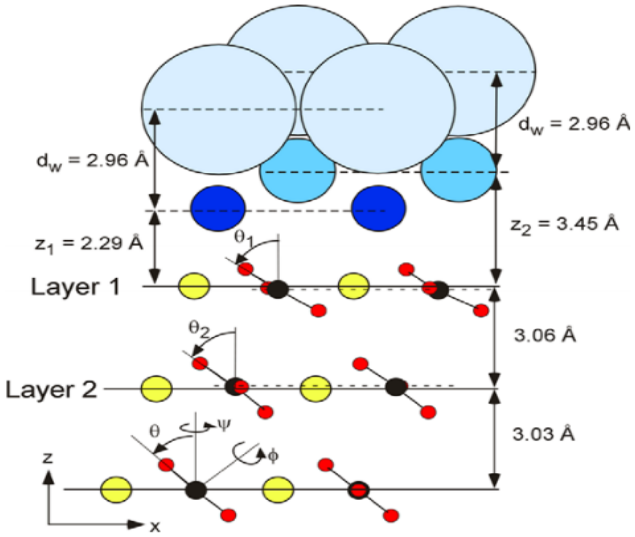

Figure 7.3: Schematic of calcite-water interface, where Ca (yellow circles), C (black circles), Oc (red circles), and the first two adsorbed water layers (blue circles) are shown. The increase in the size of the water molecules' circles represent the rise in the root-mean-square vibrational amplitudes [58].

3.45±0.2 from the calcite surface respectively. The schematic of the best-fit model is shown in Figure 7.3 for the hydration layer. They suggested that there was a chemical interaction (strong attractive force) between the calcite surface and Ow1 whereas Ow2 and calcite surface had a weaker, non-specific interaction. The water molecule Ow1 did not occupy the space directly above the Ca ion as it showed lateral displacement. It was not possible to predict the exact position of Ow2 because of its large vibrational amplitude.

They suggested that Ow2 occupied the space between the Ow1 molecules to complete the hydration layer on the calcite surface. They did not find any structuring of water layers beyond this hydration layer [58].

Moreover, Neagle et al. [62] used an infrared technique to describe calcite-water interface.

7.1.3 Adsorption of methane on kaolinite clay

Liu et al. [59] investigated the effects of high pressure on the adsorption capability of clay minerals for methane. It was concluded that the increase in pressure at low pressures increased the adsorption capacity, but at high pressures, it remained almost constant. The adsorption sites for methane were only on the external surface of kaolinite. They could not find any adsorption site between the interlayer spacing of kaolinite. The adsorption of methane decreased in the

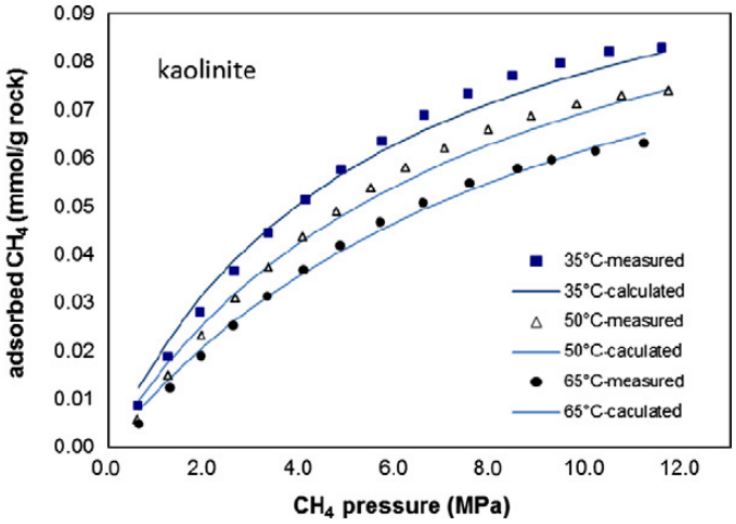

Figure 7.4: Methane adsorption in kaolinite clay, where measured amount of adsorbed methane is represented by points, and the calculated amount of adsorbed methane based on the Langmuir equation, is represented by lines [60].

presence of water as adsorbed water can accommodate adsorption sites, leaving little room for methane adsorption. Kaolinite (having a large external surface area) showed a higher adsorption capability for methane as it adsorbed less water compared to illite [59].

Ji et al. [60] studied methane adsorption on clay-rich rocks at 35 °C, 50 °C and 65 °C and pressures up to 15 MPa. The objective was to investigate methane sorption isotherms and determine which clay mineral is the dominant candidate for methane adsorption. The samples of montmorillonite, kaolinite, illite, chlorite, and interstratified illite/smectite were collected from clay-dominated rocks and then these samples were crushed to four particle sizes: 20–50 mesh, 50–100 mesh, 100–270 mesh, and larger than 270 mesh. They took the kaolinite clay sample from a kaolinite quarry in Fugu County, China, and further processed it in Carboniferous–Permian coal-bearing strata. The volume adsorption apparatus was used to perform experiments to obtain sorption isotherms for clay-methane systems. The adsorption capability of methane on clay minerals decreases in the following order montmorillonite $>>$illite/smectite mixed layer $>$kaolinite $>$chlorite $>$illite. The measured amount and the calculated amount of adsorbed methane based on the Langmuir equation on the kaolinite is shown in Figure 7.4. They documented physisorption as a dominant process for adsorption of methane in clay minerals [60].

7.2 Computer Simulations

The important findings of arrangement and interactions at the water-kaolinite interface by Tunega et al. [63] are described in Section 7.2.1.

7.2.1 Analysis of Interactions between water and kaolinite surfaces using *ab initio* MD simulation

The structure and dynamics of the monomolecular water layer was investigated on kaolinite surfaces by means of short-time *ab initio* MD. Vienna *ab initio* simulation package (VASP) was used to perform this MD. In this study, a canonical ensemble with the Nose-Hoover technique was applied where temperature was maintained at 300 K. They applied the velocity Verlet algorithm with time step of 1 fs, and the total simulation time was 4 ps. The kaolinite crystal was derived from a mineral dickite structure with unit-cell parameters as $a = 10.376\mathring{A}$, $b = 8.818\mathring{A}$, $c = 26.400\mathring{A}$ and $\beta = 96.7^{o}$. The system was built by randomly distributing nine water molecules on surfaces. A vacuum of 21 Å was left above the layer surface. They studied the difference in interactions of the octahedral and tetrahedral surfaces of kaolinite with water molecules. Another system for tetrahedral surface studies was built by the increasing number of water molecules to 36 and doubling the unit-cell parameters a and b.

The surface hydroxyl group dominates the surface interactions on the octahedral surface. The hydroxyl groups have the ability to form H-bonds both as proton donors and acceptors, whereas hydroxyl groups' configuration around octahedral holes also help to form H-bonds. Interestingly, they found was the formation of three H-bonds between one water molecule and the hydroxyl groups on the surface. The hydrogen bonding influences the structuring of the water molecules on the surface. They observed two types of hydrogen bonding: one in which water molecules act as donors and a second in which the surface hydroxyl groups act as donors. Breaking and reforming of the bond occurs during the simulation run because of mutual interactions and the thermal energy of the water molecules.

Basal oxygen atoms (surrounding the ditrigonal hole) dominate the surface interactions on the tetrahedral surface. They observed only weak interactions between the water and basal oxygen. They observed that water molecules prefer to form H-bonds among themselves by overcoming the weak interactions between water and the tetrahedral surface in the extended model where the number of water molecules was increased to 36 [63].

A number of computer simulation studies have been carried out in order to investigate the adsorption pattern of water on hydrophilic and hydrophobic surfaces of kaolinite clay [64–67].

Jin et al [68] studied the sorption of methane in clay minerals in an aqueous environment and found that the increase in pore size greatly reduced the adsorption of methane [68].

In order to understand and describe the calcite-water interaction and adsorption phenomenon, several computational techniques have previously been used [69–72].

8 Simulation Details

This section introduces the simulations details and the analysis performed in this work along with the systems (calcite and kaolinite systems) under consideration.

8.1 Calcite System

A calcite slab was built using GDIS [73] from the crystallographic information found by Markgraf et al. [74]. The rhombohedral crystal structure of calcite with space group R$\overline{3}$c has cell parameters: $a = b = 4.990\mathring{A}$, $c = 17.061\mathring{A}$, $\alpha = \beta = 90^{o}$ and $\gamma = 120^{o}$ [74]. The dimensions of the rigid wall of the calcite slab, that was cleaved at the $\{10\overline{1}4\}$ plane, were 39.9 Å x 48.6 Å x 29 Å. The system was organised with the distribution of methane (one-site model was used in this study) and water phases around the calcite surface, as shown in Figure 8.1. In this figure, the colour code is: calcite (calcium: blue, carbon: black, and oxygen: red), water (hydrogen: white and oxygen: red), and methane (carbon: green). The further details have been described in Section 8.3.

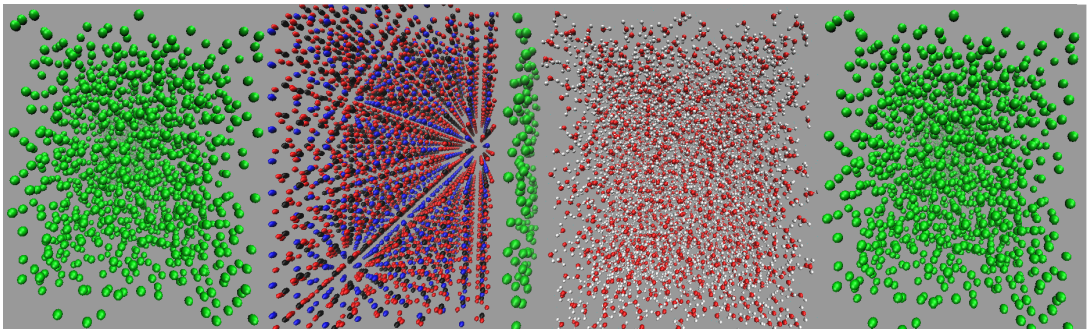

Figure 8.1: Primary cell of the calcite system: (from the left) methane (1268 atoms), calcite crystal (4800 atoms), methane (141 atoms), water (2910 molecules) and methane (1268 atoms).

The density of the compressed liquid methane used was 387 kg/m^3 at 138 K and 46.4 bar [75]. A thin phase of methane was introduced between the water phase and calcite slab on one side, while a thick methane phase was positioned before the calcite slab on the other side in order to avoid the effect of fluctuations on adsorbed methane molecules on the surface in density profile calculations due to the volume change of the primary cell. The dimensions of the resulting primary cell for simulation were 39.9 Å x 48.6 Å x 170 Å consisting of 16207 atoms.

8.2 Kaolinite System

The crystallographic details were taken from Bish [76] to build a kaolinite crystal exposing the octahedral (alumina) surface on one side and the tetrahedral (silica) surface on the other side using GDIS [73].The dimensions of the rigid wall of the kaolinite slab were 41.2 Å x 44.7 Å x 19.5 Å. This system also followed the distribution of methane (one-site model was used in this study) and water in the primary cell in the same way as described in the calcite system, but the number of molecules varied as the length along x and y directions according to the crystal slab size, as shown in Figure 8.2. In this figure, the colour code is: kaolinite (silicon: yellow, oxygen: red, aluminium: pink, and hydrogen: white), water (hydrogen: white and oxygen: red), and methane (carbon: green). The further details have been described in Section 8.3. A thin phase of methane was introduced between the water phase and octahedral surface of the crystal. The dimensions of the resulting primary cell for simulation were 41.2 Å x 44.7 Å x 165 Å consisting of 14913 atoms.

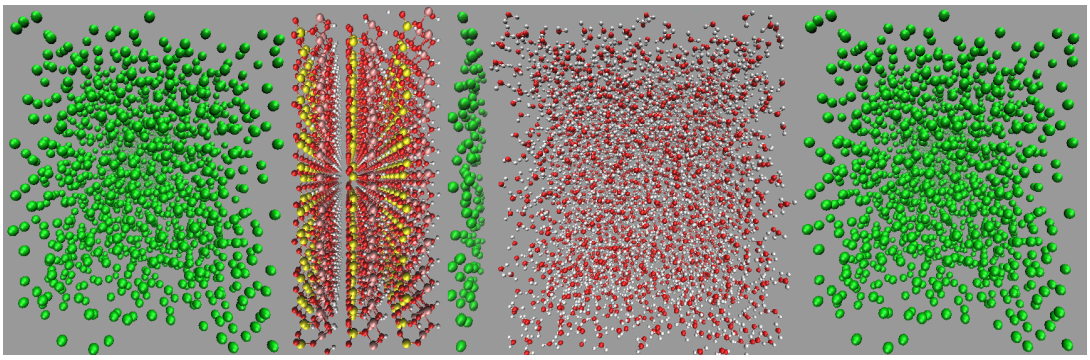

Figure 8.2: Primary cell of the kaolinite system: (from the left) methane (1205 atoms), kaolinite crystal (4080 atoms), methane (134 atoms), water (2763 molecules) and methane (1205 atoms).

8.3 Computational Details

Crystal structures and liquid phases were created separately and then combined with the help of the TopoTools plugin in VMD [81] to get the required system set up. Packmol software [82] was used to model water and methane phases whereas for crystals GDIS [73] was used. The computer code LAMMPS [83] was used to implement MD simulations to investigate the required objectives. The time step of 0.1 fs was first used for 1 ps to equilibrate the systems. The time step was then increased to 1 fs to achieve equilibrium. During the equilibration run, methane was completely replaced by water on the surfaces and thus did not affect the result analysis in

Table 8.1: Lennard-Jones Parameters for calcite and water [77].

Lennard-Jones parameters					
Pairwise L-J		ϵ (kcal/mol)	σ (Å)	A (kcal * Å^{12}/mol)	C (kcal * Å^{6}/mol)
Ca	C	0	0		
Ca	Hw	0	0		
Ca	Oc			226816.44	0
Ca	Ow	0.27	2.76		
C	Hw	0	0		
C	Oc	6.27	1.197		
C	Ow	0.116	3.469		
Oc	Hw	6.97 x 10^{-6}	4.497		
Hw	Ow	0	0		
Oc	Ow	0.146	3.119		

Table 8.2: Charge distribution on calcite [77].

Charge distribution			
	Ca	Oc	C
charge	1.668	-0.889	0.999

Table 8.3: Parameters for one-site methane model [78].

Lennard-Jones parameters			Charge distribution
L-J pure	ϵ (kcal/mol)	σ (Å)	charge
Cm	0.294	3.73	0.0

Table 8.4: Parameters for TIP3P water model [79].

Lennard-Jones parameters				Charge distribution	
Pairwise L-J		ϵ (kcal/mol)	σ (Å)	charge	
Ow	Ow	0.102	3.188	Ow	-0.834
Hw	Hw	0	0	Hw	0.417
Ow	Hw	0	0		
Bond Parameter				**Angle Parameter**	
Bond		k$_s tr$ (kcal/mol)	r$_e$ σ	Angle	k$_a ng$ (kcal/mol)	$\theta_e(^o)$
Ow – Hw		450	0.9572	Hw – Ow – Hw	55	104.52

Table 8.5: Parameters for kaolinite [80].

Lennard-Jones parameters			Charge distribution
Pure L-J	ϵ (kcal/mol)	σ (Å)	charge
Alk	1.33 x 10 ≏6	4.2713	1.575
Ohk	0.1554	3.1655	-0.95
Hkm	0	0	0.425
Hk	0	0	0.425
Sik	1.84 x 10^{-6}	3.302	2.1
Ok	0.1554	3.1655	-1.05

this respect. The total equilibration time was 0.501 ns. The integration method used in this study was the velocity Verlet algorithm. The production run lasted for 1.5 ns using a time step of 1 fs with the trajectory details output to .DCD files at 0.001 ns (1ps) intervals. The NPT ensemble was applied on this system, maintaining temperature at 273 K and pressure (in the z-direction) at 100 bar. Nose-Hoover thermostat and barostat was used to maintain temperature and pressure conditions in this ensemble. Periodic boundary conditions were applied in all three directions. The L-J potential was used to model the short-range molecular interactions with a cut-off distance of 10 Å whereas P^3M was used to evaluate electrostatic interactions. The atoms of calcite and kaolinite slabs were kept fixed at their crystallographic positions. The parameters used to calculate the potential energy of the systems in this study are given in Tables 8.2 - 8.5. Geometric mixing rules was used to calculate the L-J parameters (that are not listed in Tables) between pure species. The SHAKE algorithm was used to restore the original bond length and angle of water molecules at each time step. Bond and angle potential contributions were included in these simulations based on harmonic style.

8.4 Results Analysis

The H-bond plugin was used to evaluate the H-bonds formation as one of the ways to analyse one effect of the mineral-water interactions. The number of H-bonds were calculated at different cut-off distances (2.5 Å, 2.8 Å, 3 Å, 3.2 Å) with a cut-off angle of 150°. The cut-off distance is the distance between the atom (e.g., D) that is covalently bonded to the hydrogen atom and atom (e.g., A) that forms the interaction with hydrogen (D—H..A). In order to determine the existence of an H-bond the geometric criteria used are as follows:

1. The presence of a hydrogen donor and a hydrogen acceptor.

2. The hydrogen donor and acceptor should be at a given cut-off distance.
3. The angle (D—H..A) must be within a given cut-off angle .

To determine the distribution of molecules or atoms in the primary cell, the density profile tool was used to obtain mass density of the molecules and atoms along the z-direction. The distance of 20 Å from the surfaces for density profiles was considered in plotting graphs if not stated in the figures.

All the graphs have been plotted using the MATLAB program. In the calcite system, the distance was taken as zero at the position of the calcium ions at the top surface layer, whereas the average positions of the surface oxygen atoms of the respective surfaces were taken at distance zero in the kaolinite system. It must be taken into account in the density profile analysis that methane was found primarily as a separate phase during the simulation with a few dispersed methane molecules in the water phase.

9 Results and Discussions

The primary focus of this analysis is to describe structure and hydrogen bonding of water at the mineral and water interface as well as the possibility of heterogeneous nucleation of methane hydrates. Calcite and kaolinite system are discussed in Section 9.1 and 9.2, respectively. In Section 9.3, a brief comparison between these systems is reported.

9.1 Calcite System

The presence of an aqueous environment on the calcite surface caused minor distortions of calcium and CO_3 ions from their ideal bulk positions in the outermost layer in which displacement in the positions of calcium and CO_3 groups, and small rotations of CO_3 groups was observed by X-ray experiments [58]. In these simulations, the lattice was rigid, as the first approach was approximated since it is much more computationally efficient, and it was more important to obtain a first impression of the possible adsorption structures. If the results appeared to deviate in important aspects related to this approximation, then simulations could be repeated with flexible ionic bonds in the mineral.

9.1.1 Structuring of water and methane on the calcite surface

Initially methane adsorbed directly onto the calcite surface despite the absence of partial charges in the one-site L-J model for methane. As simulation progressed, methane and water competed to adsorb on the calcite surface. Water completely replaced methane from the surface since calcite preferred to adsorb water. The water adsorption pattern of the first two layers appeared significantly influenced by the presence of methane, and the time needed to replace the methane completely was about 0.4 ns. The primary layer of water on the calcite-water interface displayed a height at a distance of 2.28 Å from the surface calcium ion which is comparable to the experimental and theoretical outcomes shown in Table 9.1. The height of the next layer that was more organised than the bulk water was found at a distance of 3.48 Å. The strong interactions between water and the calcite surface are discussed on the basis of hydrogen bonding in Section 9.1.2. The distance between the first and second adsorbed layers of water on the surface was very small, so there was no place for methane to stay there. The presence of methane was observed after the second adsorbed layer and a rising trend outside of 6Å from the calcite surface was quite obvious as shown in Figures 9.2 and 9.3. Methane as a separate phase got trapped here. Its position oscillated between 7 Å and 31 Å from the surface. Methane could not escape through

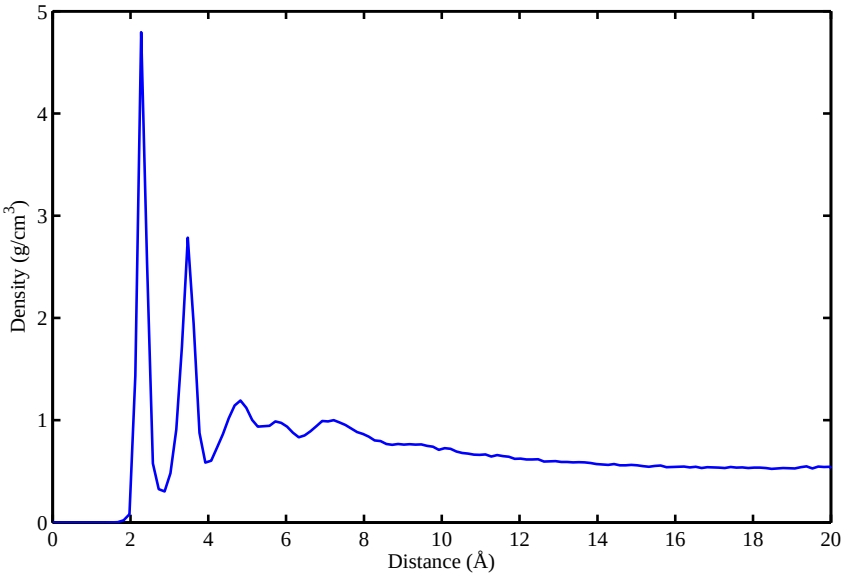

Figure 9.1: Density of water on the calcite surface.

water phase within the time span covered in this work. Methane molecules that became trapped here were mainly the ones that were introduced between the calcite surface and water phase to check their behaviour under such circumstances. Very few dispersed methane molecules were found in the water phase, as expected by the general low solubility. The complete distribution of methane and water in the primary cell is shown in Figure 9.3.

The X-ray scattering experiments did not show any structuring beyond the first two monolayers of water molecules [58], but the MD results found the effect of calcite surface on water with two more adsorbed layers [84]. In this study the ordering of water beyond the first two layers was witnessed by the existence of two small peaks at a distance of 4.83 Å and 7.23 Å.

As seen in Table 9.1, the sampled results from the model system simulation are comparable with the experimental data.

9.1.2 Calcite-water interface analysis in terms of hydrogen bonding

The number of H-bonds formed between water molecules and atoms on the calcite surface was studied. The geometrical criteria used to determine the existence of H-bonds are described in Section 8.4.

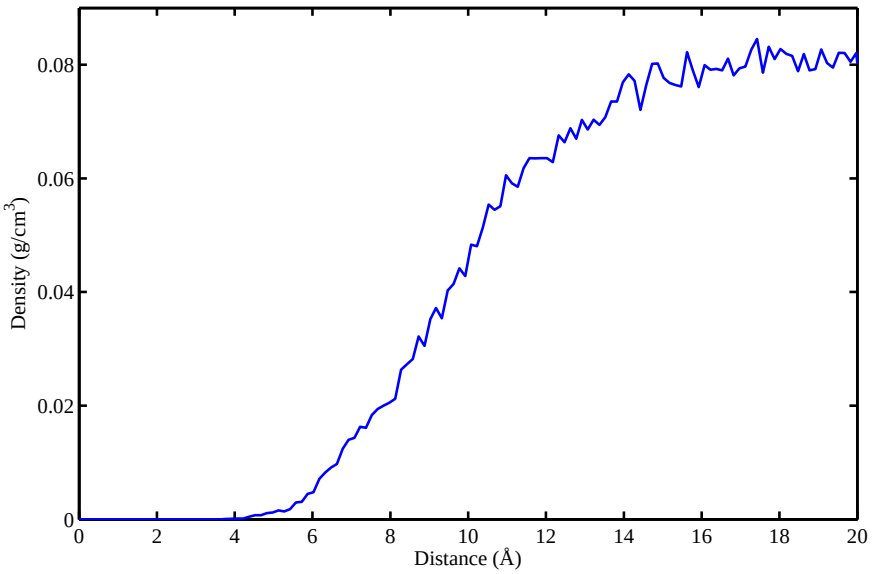

Figure 9.2: Density of methane on the calcite surface.

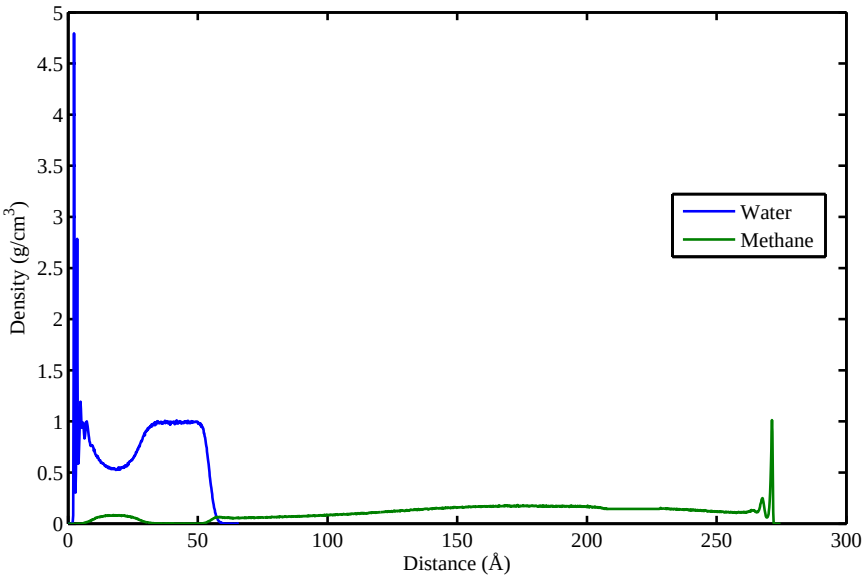

Figure 9.3: Density of methane and water on the calcite surface in the primary cell.

Table 9.1: Comparison of experimental and theoretical outcomes The position of water layers on the calcite surface; where z=0 at the calcium ions of the top surface layer.

Method	First layer (Å)	Second layer (Å)	Third layer (Å)
X-ray scattering [85]	2.5±0.12		
X-ray scattering [58]	2.3±0.1	3.45±0.2	5.25
MD simulation [86]	2.3	3	5.0
MD simulation [84]	2.2	3.2	5
This study	2.28	3.48	4.83

As the interactions between the surface calcium ion and oxygen atom of the water molecule were described as ionic by Villegas-Jimenez et al. [87], the interactions that were obtained satisfying the hydrogen bonding criteria would be regarded as Coulombic forces of attractions (or Coulombic interactions) between the surface calcium ion and oxygen atom of water molecule. The calcium ion and oxygen atom formed maximum attractions when both were very close to each other as shown in Figure 9.4, in which the Coulombic interactions mainly occurred when surface calcium ion was at a distance of less than 2.5 Å from the oxygen of the water molecule. As oxygen atoms of first adsorbed layer mainly occupied the positions at a distance of 2.28 Å (in z-direction) from the surface, very few oxygen atoms were occupying the space between the density peaks of the first two adsorbed layers, which is quite evident from the atomic density profile of oxygen in Appendix A.1. Furthermore, there was no increase in the number of interactions between the cut-off distance of 2.8 Å and 3.2 Å. If only the distance between calcium and oxygen is considered, the interactions formed with a value of bond energy between -15 and -40 kcal/mol, are very strong, as mentioned in Table 6.1. As an aqueous environment can lead to the dissolution of the calcite surface [71], these interactions can be the primary contributor in destroying the crystal lattice resulting in formation of calcium hydroxide. It was found that oxygen atoms in the first water layer did not occupy the positions directly above the surface calcium ion, and located little displaced in the x-direction and y-direction with respect to the surface calcium position. Geissbuhler et al. [58] reported similar observations, as shown in Figure 7.3. The average bond length between the surface calcium ion and oxygen of the water (Cac_Ow) was calculated to be $\approx$ 2.43 Å which is comparable to the theoretical results [70, 71, 87]. One surface calcium ion adsorbed water molecules by forming interactions with 1.3 oxygen atoms on average (at a cut-off distance 2.5 Å) of the first water layer which is a slightly higher value in comparison to 0.99-1.15 reported by Wolthers et al. [70]. The differences in force fields that were used could be the reason for this slight disagreement. Furthermore, the simulation in this study was conducted at a low temperature and high pressure.

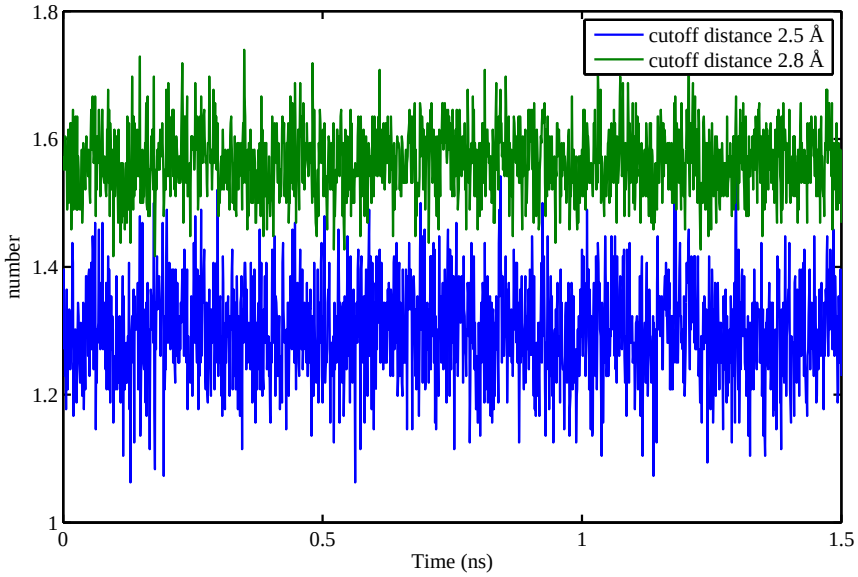

Figure 9.4: Sampled Coulombic interactions between oxygen atom of the water and surface calcium ion, where number represents number of oxygen atoms coordinated per surface calcium ion.

The H-bond formation between the surface oxygen atom and the hydrogen atom of the water molecules was also examined in more detail.

Surface oxygen atoms formed maximum hydrogen bonding interactions when the distance between the proton donor (oxygen atom of water) and acceptor (surface oxygen atom) was greater than 2.8 Å; thus, these bonds were not as strong as the previous ones. In this case, the energy of interaction was around -4 kcal/mol, as shown in Table 6.1, whereas the number of H-bonds formed per surface oxygen atom was 1.48 on average at a distance cut-off of 3.2 Å, which is higher compared to the calculated average value of 1.23 by Wolthers et al. [70]. The surface carbon atom which was keeping the carbonate group intact, developed a very small number of interactions with the water molecules at a cut-off distance 3.2 Å as shown in Figure 9.6. The carbon atom was surrounded by three oxygen atoms of calcite; thus, the chances of its interaction were very low.

In summary, the surface carbon atom contributed substantially less towards adsorbing water molecules. The calcite surface adsorbed the first layer of water mainly due to the two forces of attractions: Coulombic interactions between the surface calcium ion and oxygen atom of the water and the hydrogen bonding attraction between the surface oxygen atom and hydrogen atom of the water.

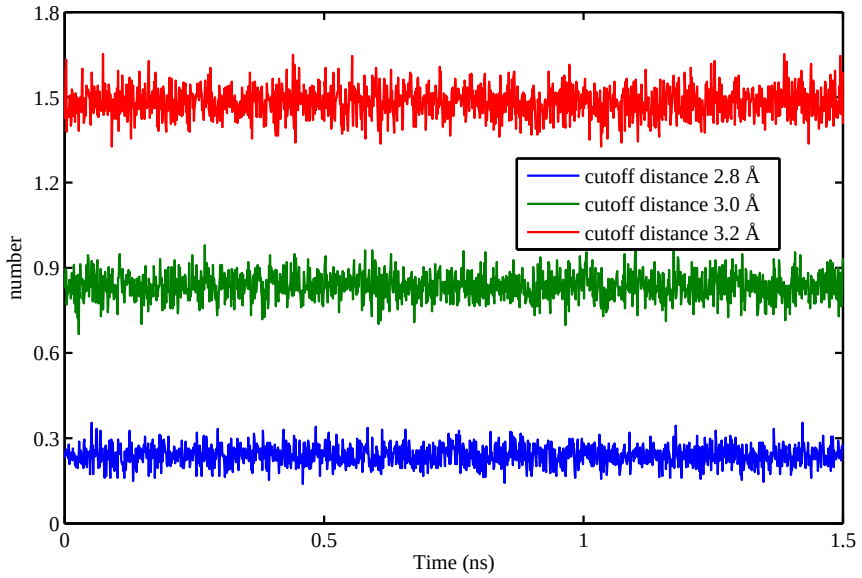

Figure 9.5: Sampled hydrogen bonds between hydrogen atom of the water and oxygen atom of the calcite surface, where number represents number of hydrogen bonds formed per surface oxygen atom.

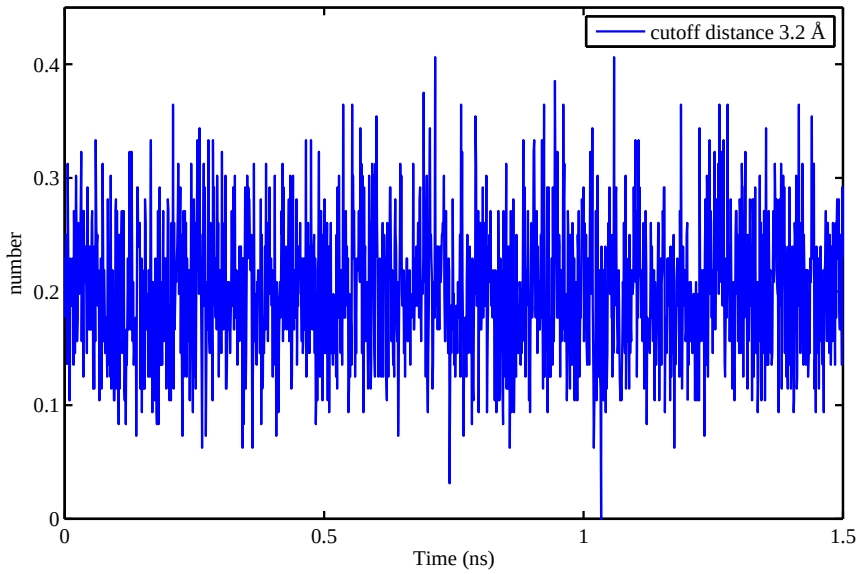

Figure 9.6: Sampled Coulombic interactions between oxygen atom of the water and surface carbon atom, where number represents number of oxygen atoms coordinated per surface carbon atom.

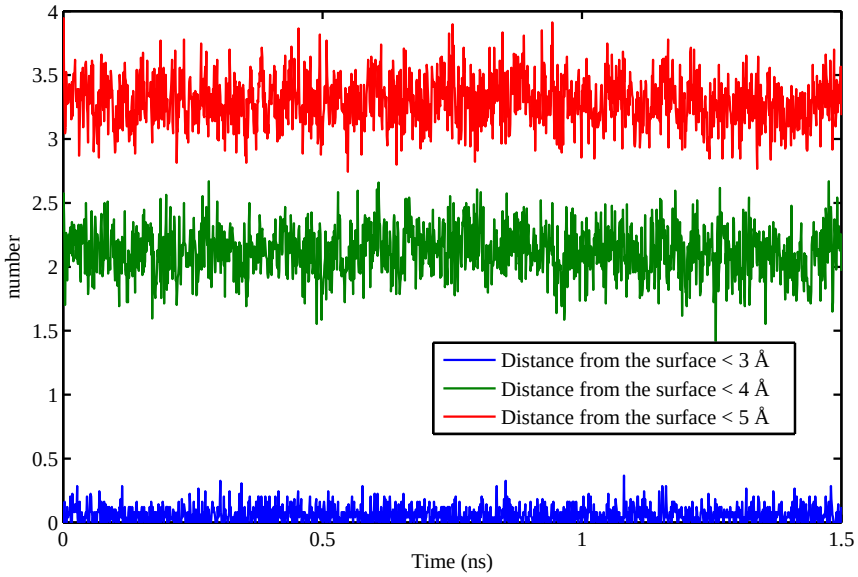

Figure 9.7: Sampled hydrogen bonds between water molecules on the calcite surface at different cutoff distances, where number represents number of hydrogen bonds formed per water molecule.

The effect of the calcite surface on the hydrogen bonding network between the water molecules in the adsorbed layers is shown in Figure 9.7. There were almost no H-bonds between the water molecules when observed at a distance of less than 3 Å from the surface, indicating that, in the first layer, this network was completely distorted by strong calcite-water interactions. At a distance of less than 4 Å, the hydrogen bonding network recovered a little. Water molecules of the second layer might have formed bonds with each other and with the first adsorbed layer. Villegas-Jimenez et al. [87] also documented the absence of an H-bond network in the first layer between water molecules as a result of chemisorption on the surface and observed that the second layer of water formed H-bonds with water molecules present in the first layer and oxygen atoms of the calcite surface [87]. The hydrogen bonding network was almost completely reclaimed at a distance of less than 5 Å from the surface.

9.1.3 Heterogeneous hydrate nucleation on the calcite surface

The distance between the first and second adsorbed layers of water on the calcite surface was very small, thus providing no room for methane molecules to stay there, but the slightly broader gap between the second and third layers allowed more room to accommodate the methane, which can be seen in Figure 9.2. Methane as a separate phase got trapped in that region; therefore, it

was difficult to imagine the number of dispersed methane molecules in the surrounding water phase through the density profile. Very few dispersed methane molecules were also found in the water phase, as expected by the general low solubility. The position of the trapped phase oscillated between distances of 7 Å and 31 Å from the surface. The calcite surface allowed contact between the water and the methane (in both the disperse and separate phases) that could be a precursor of nucleation. Substantially longer simulation times will be needed to obtain a clearer picture of that aspect. Since the periodic boundary condition is utilised the regularity imposed by the copied central box might also counteract structural rearrangements towards hydrate nuclei. Substantially larger simulation systems might be a way to move forward. This was outside the reach of the computational resources available for this project but the utilisation of a very fast graphical processing unit (GPU) might open up better possibilities in follow-up projects.

9.2 Kaolinite System

A realistic periodic boundary system containing representative distributions of all atoms present would require a system larger than what could be reasonably handled within the CPU computational resources available for the project. Although strictly in contrast with the rules of PBC, a crystal consisting of an aluminium (Al) dominated structure on one side and a silicon (Si) dominated surface on the other side was constructed as a first approach. The best option would likely be to study two different cuts of the crystal separately with similar consistent boundary conditions for an Al-exposed surface and Si-exposed surface for the two systems. Strictly speaking cuts could be made so that the two simulation systems could be constructed: one Si-based and one Al-based system. This would have been a natural follow-up, if time had permitted. However, as mentioned, this was a starting system to obtain a first picture of the adsorption patterns with a focus on the possible solid/water/methane structures that potentially could lead to nucleation of hydrates, if a simulation could run long enough.

9.2.1 Structuring of water and methane on kaolinite surfaces

In the beginning, water molecules first moved towards the Al side, but many of the water molecules changed direction towards the Si surface. There could be two reasons for the movement of water molecules towards the Si surface. First, water molecules moved all the way through the methane to become adsorbed on the tetrahedral surface. Second, the adsorption capability of kaolinite for methane molecules increased under high pressure and low temperature conditions as observed by Ji et al. [60] and thus penetrated in order to reach the octahedral

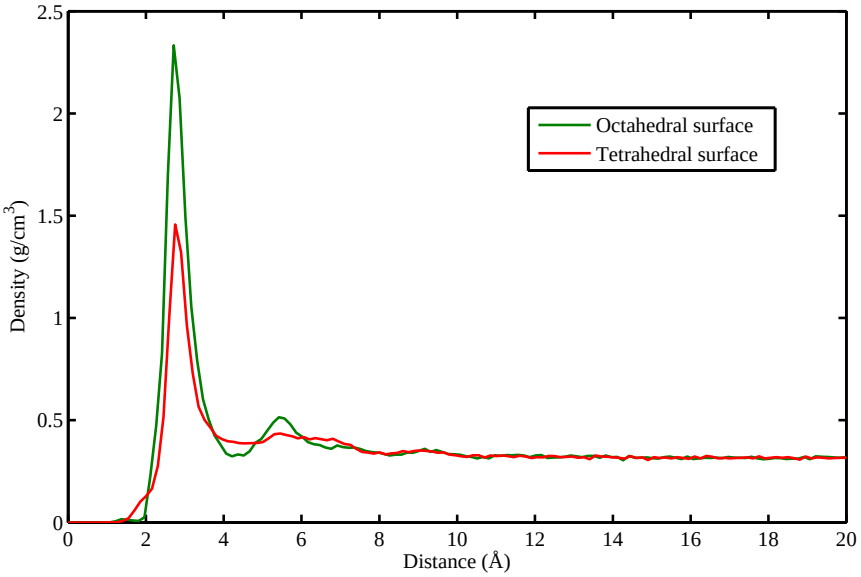

Figure 9.8: Density of water on the kaolinite surfaces.

surface. To understand the real reason behind this phenomenon, a larger system would need to be built in the future.

Water formed two structured layers on the octahedral surface; one is significant while the other is small, as shown in Figure 9.8. The heights of the first and second adsorbed water layers were at a distance of 2.72 Å and 5.42 Å from the octahedral surface. The surface hydroxyl group, which was acting as both a proton acceptor and donor, played the main role in adsorbing water as described in Section 9.2.2. The ability of the tetrahedral surface to adsorb water was low compared to that of the octahedral surface. Only one adsorbed layer of water was found at a distance 2.76 Å from the surface, while no structuring of water was found beyond this layer. The peak of first adsorbed layer of water on octahedral and tetrahedral surfaces was in good agreement with theoretical studies as shown in Table 9.2.

Methane demonstrated a denser first layer on the tetrahedral surface than that on the octahedral surface, as shown in Figure 9.9. The reason might be the relatively non-polar nature of the tetrahedral surface and the absence of the hydroxyl group on the surface. The primary adsorption layer was formed by water, whereas methane formed the secondary layer on both surfaces. The density peaks of methane on the octahedral and tetrahedral surfaces was at a distance of 3.32 Å (the distance from the first water layer is 0.6 Å) and 3.21 Å (the distance from the first water layer is 0.45 Å), respectively, from the surfaces. Methane formed three significant structured

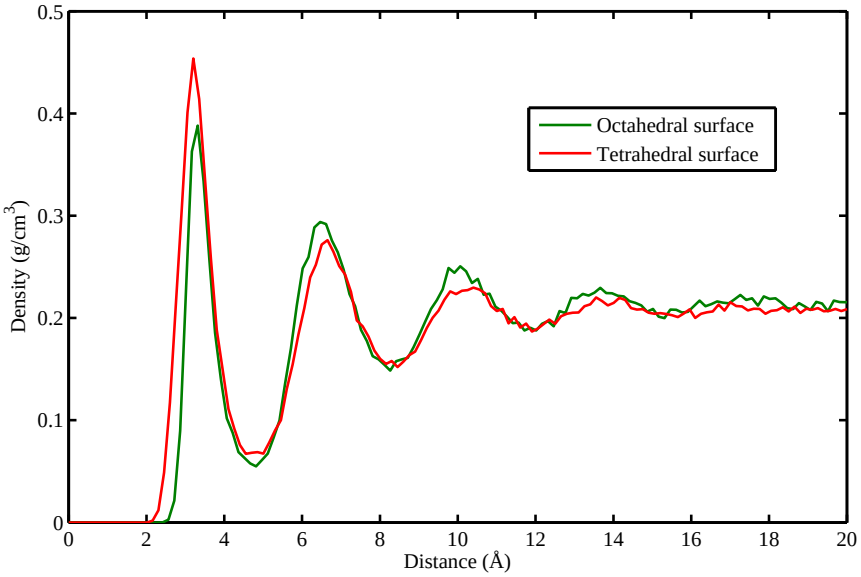

Figure 9.9: Density of methane on the kaolinite surfaces.

layers on these surfaces.

9.2.2 Kaolinite-water interface analysis in terms of hydrogen bonding

At cut-off distance of 2.5 Å, no h-bonding between water and kaolinite surfaces was detected. On the octahedral surface, there was no interaction between the surface Al and oxygen of the water molecule at a cut-off distance of 3.2 Å. The hydroxyl groups on the octahedral surface provided interaction sites for water molecules. When the surface hydroxyl group acted as a proton acceptor, surface oxygen atoms formed H-bonds with hydrogen atoms of the water as shown in Figure 9.10. As the distance between the proton donor (oxygen atom of the water) and acceptor (surface oxygen atom) increased, more interactions developed. The bonds with the energy value around -4 kcal/mol were weak, as mentioned in Table 6.1. The average number of H-bonds formed per surface oxygen atom was 0.74 at a distance cut-off of 3.2 Å.

As the octahedral surface has a hydroxyl group, the hydrogen atom also contributed in creating interactions. The number of H-bonds formed by the surface hydrogen atom with an oxygen atom of water is shown in Figure 9.11. In the preferred adsorption structure, the surface hydroxyl group formed one H-bond as an acceptor (which is stronger) and two as a donor with bond lengths of 1.73 Å and $\approx$ 2 Å, respectively, as described by Hu et al. [90]. In this study, the surface

Table 9.2: Comparison of theoretical results of atomic density peaks of oxygen atoms of the water on the kaolinite surfaces, where z=0 at average position of oxygen atoms of respective surface on the top layer.

Surface	Method	First peak (Å)	Second peak (Å)
Octahedral	Molecular dynamics study [88]	2.6-2.9 [a]	
	Molecular dynamics study [89]	2.55	5.10
	This study	2.73	5.43
Tetrahedral	Molecular dynamics study [88]	2.5-3 [b]	
	This study	2.76	

[a] The range was obtained from SPC/E and TIP4P water models.

[b] The range was obtained from SPC, SPC/E and TIP4P water models.

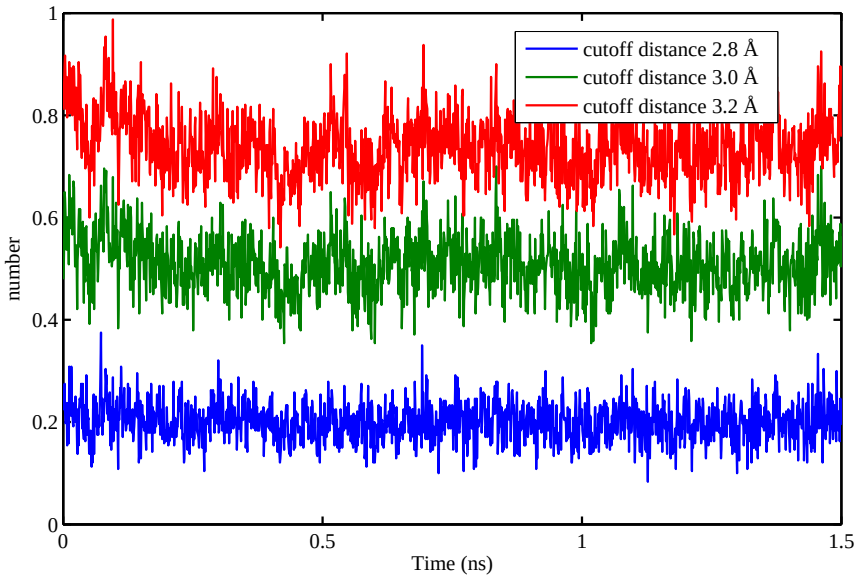

Figure 9.10: Sampled hydrogen bonds between hydrogen atom of the water and oxygen atom of the octahedral surface, where number represents number of hydrogen bonds formed per surface oxygen atom.

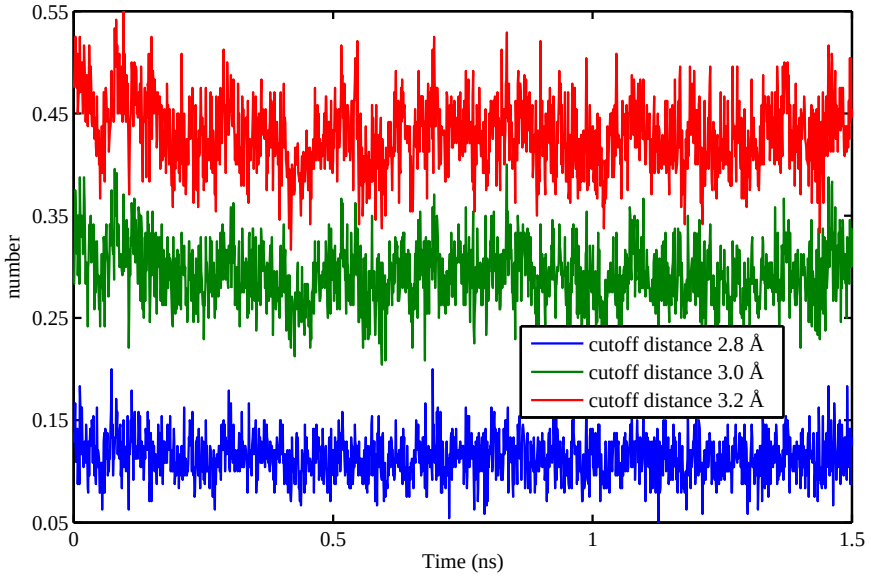

Figure 9.11: Sampled hydrogen bonds between oxygen atom of the water and hydrogen atom of the octahedral surface, where number represents number of hydrogen bonds formed per surface hydrogen atom.

hydroxyl group showed less ability to donate proton by creating 0.43 H-bonds per hydroxyl group at cut-off distance of 3.2 Å. This number rose to 0.74 when it acted as an acceptor under the same conditions. The surface hydroxyl group acting as both a proton acceptor and donor at the kaolinite-water interface, was also observed in theoretical studies [63, 88, 90]. Hence, the presence of the hydroxyl group was an important aspect of adsorption of water on the octahedral surface.

On the other hand, the tetrahedral surface developed weak interactions with water. Silicon did not establish attractive forces with water molecules. Only oxygen atoms of the tetrahedral surface acted as a hydrogen acceptor to form bonds with water molecules, as shown in Figure 9.12. The average number of H-bonds formed per oxygen atom of the tetrahedral surface at the cut-off distance of 3.2 Å was 0.48, which was slightly higher than the interactions formed by hydrogen atom of the octahedral surface. Tunega et al. [63] noticed the bond breaking and reforming on the surface during simulation run [63]. The fluctuation in the number of H-bonds formed was also evident in this system, as demonstrated by Figures 9.10-9.12.

The main purpose of showing H-bonds formed at the water-kaolinite interface was to differentiate between the characteristics of the octahedral and tetrahedral surfaces in an aqueous

environment. It proved the hydrophobic nature of the tetrahedral surface compared to the hydrophilic octahedral surface.

9.2.3 Heterogeneous hydrate nucleation on kaolinite surfaces

Three structured layers of methane on kaolinite surfaces were found, which was quite different behaviour in comparison to the water that experienced only one significant layer (also a second small peak on the octahedral surface). The density depth after the first adsorbed layer of water yielded space for methane. Kaolinite surfaces provided good adsorption sites for methane and thus provided contact between the water and methane, which can be a precursor of nucleation. It is hard to predict anything specifically from this system as described in the beginning of Section 9.2.

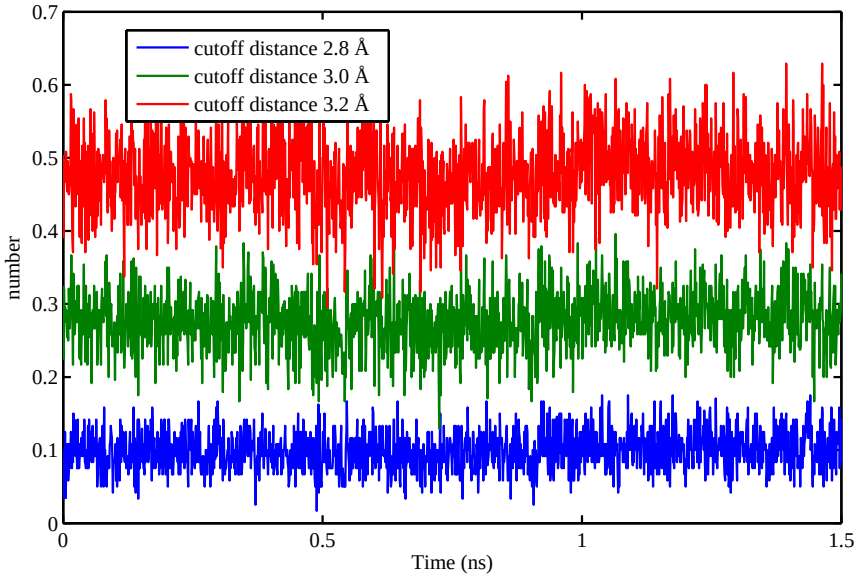

Figure 9.12: Sampled hydrogen bonds between hydrogen atom of the water and oxygen atom of the tetrahedral surface, where number represents number of hydrogen bonds formed per surface oxygen atom.

9.3 Calcite surface vs Kaolinite surfaces

Water adsorbed well on the calcite surface as a result of strong attractive forces developed at the calcite-water interface. The two dense layers on the calcite surface did not provide any

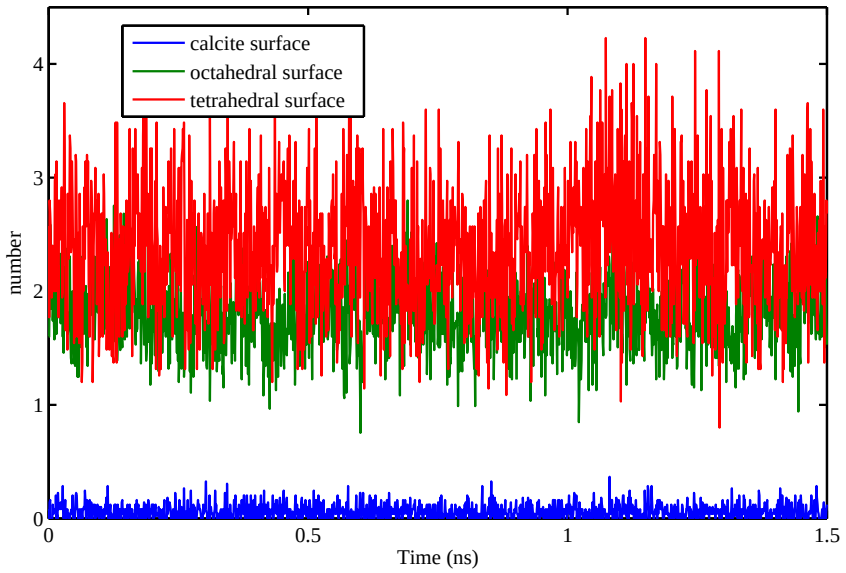

Figure 9.13: Comparison of sampled hydrogen bonds between water molecules at distance less than 3 Å from respective surfaces.

room to accommodate methane molecules. Strong attractions displaced all methane molecules from the surface. The interactions between water and kaolinite surfaces were weaker compared to the interactions at calcite-water interface. Methane molecules benefited from these lower interactions and reached the surface.

To adsorb water molecules effectively, solid-water interactions should overcome the hydrogen bonding network between water molecules.

Smith et al. [91] calculated the average number of H-bonds in liquid water to be 3.3 [91]. There was almost no hydrogen bonding network between water molecules when observed at a distance of less than 3 Å from the calcite surface. The average number of H-bonds formed per water molecule between molecules of the first layer was 0.06. In contrast to the behaviour of the calcite surface, kaolinite surfaces disturbed the hydrogen bonding network between water molecules of the first layer to some extent, and 1.81 and 2.38 H-bonds on average per water molecule were found on the octahedral and tetrahedral surfaces, respectively. This witnessed lower attraction for the tetrahedral surface compared to the hydrophilic octahedral surface. A comparison of the hydrogen bonding network between water molecules near these surfaces is shown in Figure 9.13.

The thin phase of methane was introduced between the water and surfaces in order to investigate

its behaviour. In the calcite system, methane molecules (of thin phase) became trapped after the third adsorbed layer of water, but no significant inclusion from methane molecules of thick phases was observed. In the kaolinite system, methane molecules of thick phases reached the surface and formed secondary layers on the octahedral and tetrahedral surfaces. For heterogeneous hydrate nucleation, the kaolinite system could provide a better environment, whereas the calcite system showed the possibility of hydrate nucleation by trapping methane molecules but contact between water and methane was very low compared to that in the kaolinite system.

10 Conclusion

In this study, MD simulation was used to investigate the possibility of heterogeneous nucleation of methane hydrates on calcite $\{10\bar{1}4\}$ and kaolinite $\{001\}$ surfaces at 273 K and 100 bar. The atoms of these surfaces were kept fixed at their crystallographic positions. Structuring of water and methane was discussed in detail on these surfaces along with the possible trap of methane molecules for heterogeneous hydrate nucleation. In the kaolinite system, the different chemical nature of octahedral and tetrahedral surfaces was also investigated.

It was concluded that surface calcium ions and oxygen atoms of the calcite played the main role in adsorbing water. The strong attractions that were formed between the calcite surface and water displaced all methane molecules (that were already adsorbed) from the surface. The hydrogen bonding network was completely distorted between water molecules in the first adsorbed layer. The surface calcium ion developed very strong attractions that could lead to calcite dissolution under suitable conditions. The density peaks of the first and second adsorbed layers of water were found at distances of 2.28 Å and 3.48 Å from the surface, respectively, which are in close agreement with experimental and theoretical studies. In this study, the ordering of water beyond the first two layers was also noticed by the presence of two small peaks. The gap between the second and third layers of water yielded some space to accommodate methane, which is possibly the precursor of heterogeneous hydrate nucleation.

In the kaolinite system, the octahedral surface developed good interactions with water but not as strong as the calcite surface established. The interactions at the solid-water interface distorted the hydrogen bonding network between water molecules to some extent in the first adsorbed layer. The surface hydroxyl group acting as both a proton donor and acceptor formed H-bonds with water. It demonstrated low ability to donate protons by forming 0.43 H-bonds on average per surface hydroxyl group at the cut-off distance of 3.2 Å compared to 0.74 H-bonds when acting as a proton acceptor. The heights of the first and second adsorbed layers of water were at distances of 2.72 Å (significant peak) and 5.42 Å (small peak) from the octahedral surface. The gap between these two layers yielded space to accommodate methane, which is possibly the precursor of heterogeneous hydrate nucleation.

The tetrahedral surface developed poor interactions with water, and only the surface oxygen atom acting as a proton acceptor formed hydrogen bonding attractions with water. It established an average of 0.48 H-bonds per surface oxygen atom at the cut-off distance of 3.2 Å. Water formed only one layer at a distance of 2.76 Å from the surface. The solid-water interface disturbed the hydrogen bonding network between water molecules in the first adsorbed layer but this distortion was lower compared to that on the octahedral surface.

In summary, the possibility of hydrate nucleation appeared to be greater in the kaolinite system compared to the calcite system. Both surfaces could initiate heterogeneous hydrate nucleation if conditions are suitable.

11 Suggestions for Further Work

There will always be aspects that could have been done differently as well as many other aspects that would have been worthwhile to investigate. Some of them are listed below.

11.1 Effects of Salt

As calcite and kaolinite are important minerals in oil and gas reservoirs [21, 22] and gas hydrate sediments [20, 23, 24], detailed studies on these minerals would be a good option to explore further concerning enhanced oil recovery, carbon dioxide sequestration, and production from gas hydrates. In particular, it would be important to investigate how ion content (salinity of injection water and groundwater) affects the adsorption and structure of water and other components.

11.2 Simulation Setup

Although strictly in contrast with the rules of PBC, a crystal consisting of an aluminium (Al) dominated structure on one side and a silicon (Si) dominated surface on the other side was constructed as a first approach. But the better option would be to keep different cuttings of the crystal in separate simulation systems so that periodic boundary conditions are fulfilled. The initial system setup in this work was, as mentioned, just a small system to obtain an initial indication even though the rules of periodicity are violated by the two different cuts on the two sides.

The concentration of thin phase of methane that was introduced between water and the solid surface should be decreased to see whether more methane molecules would disperse in water phase.

11.3 Improving the Model

Although the structuring of water on the calcite surface that was obtained in this study shows good agreement with experimental and theoretical results, it is recommended to use flexible calcite to interpret results in a more realistic manner. Simulation time in this study was very short in order to obtain any reasonable heterogeneous hydrate nucleation; thus, large simulation times would be a better choice.

11.4 Quartz

Quart, a sand forming mineral, is very important mineral in gas hydrate-bearing sediments. A similar study as conducted for calcite and kaolinite should be repeated for quartz.

References

[1] S.-Y. Lee and G.D. Holder. Methane hydrates potential as a future energy source. *Fuel Processing Technology*, 71(1):181–186, 2001.

[2] J. Murray and D. King. Climate policy: Oil's tipping point has passed. *Nature*, 481(7382):433–435, 2012.

[3] M. Höök, R. Hirsch, and K. Aleklett. Giant oil field decline rates and their influence on world oil production. *Energy Policy*, 37(6):2262–2272, 2009.

[4] L. Buryakovsky, N.A. Eremenko, M.V. Gorfunkel, and G.V. Chilingarian. *Geology and geochemistry of oil and gas*, volume 52. Elsevier, 2005.

[5] A. Demirbas. Methane hydrates as potential energy resource: Part 1–importance, resource and recovery facilities. *Energy Conversion and Management*, 51(7):1547–1561, 2010.

[6] A. Demirbas. *Methane gas hydrate*. Springer Science & Business Media, 2010.

[7] M. Levi. Climate consequences of natural gas as a bridge fuel. *Climatic change*, 118(3-4):609–623, 2013.

[8] S.-M. Lu. A global survey of gas hydrate development and reserves: Specifically in the marine field. *Renewable and Sustainable Energy Reviews*, 41:884–900, 2015.

[9] K.A. Kvenvolden. Methane hydrate—a major reservoir of carbon in the shallow geosphere? *Chemical Geology*, 71(1-3):41–51, 1988.

[10] A.V. Milkov. Global estimates of hydrate-bound gas in marine sediments: how much is really out there? *Earth-Science Reviews*, 66(3):183–197, 2004.

[11] Y.F. Makogon, S.A. Holditch, and T.Y. Makogon. Natural gas-hydrates—a potential energy source for the 21st century. *Journal of Petroleum Science and Engineering*, 56(1):14–31, 2007.

[12] K.A. Kvenvolden. Gas hydrate and humans. *Annals of the New York Academy of Sciences*, 912(1):17–22, 2000.

[13] B. Metz, O. Davidson, H. De Coninck, M. Loos, and L. Meyer. Carbon dioxide capture and storage. *(Intergovernmental Panel on Climate Change, USA)*. 2005.

[14] S.M. Benson and D.R. Cole. Co2 sequestration in deep sedimentary formations. *Elements*, 4(5):325–331, 2008.

[15] K.H. Cole, G.R. Stegen, and D. Spencer. The capacity of the deep oceans to absorb carbon dioxide. *Energy conversion and management*, 34(9-11):991–998, 1993.

[16] J. Husebø, A. Graue, B. Kvamme, J. Stevens, J.J. Howard, and B.A. Baldwin. Experimental investigation of methane release from hydrate formation in sandstone through both hydrate dissociation and co2 sequestration. In *Proceedings of the 6th International Conference on Gas Hydrates, Vancouver, British Columbia, Canada*, pages 6–10, 2008.

[17] T. Kuznetsova, B. Kvamme, K. Morrissey, T.E. Simos, and G. Maroulis. An alternative for carbon dioxide emission mitigation: in situ methane hydrate conversion. In *AIP Conference Proceedings-American Institute of Physics*, volume 1504, page 772, 2012.

[18] Y.F. Makogon. Natural gas hydrates–a promising source of energy. *Journal of Natural Gas Science and Engineering*, 2(1):49–59, 2010.

[19] J.F. Gabitto and C. Tsouris. Physical properties of gas hydrates: A review. *Journal of Thermodynamics*, 2010:1–12, 2010.

[20] N.M. Rodriguez, C.K. Paull, and W.S. Borowski. 30. zonation of authigenic carbonates within gas hydrate-bearing sedimentary sections on the blake ridge: offshore southeastern north america. In *Proceedings of the Ocean Drilling Program, Scientific Results*, volume 164, page 30, 2000.

[21] W.M. Ahr. *Geology of carbonate reservoirs: the identification, description and characterization of hydrocarbon reservoirs in carbonate rocks*. John Wiley & Sons, 2011.

[22] H. Chamley. *Clay sedimentology*. Springer Science & Business Media, 2013.

[23] C.K. Paull et al. (27 co authors). Proceedings of the ocean drilling program, vol. 164, initial reports, gas hydrate sampling on the blake ridge and carolina rise. Ocean Drilling Program, 1996.

[24] T.S. Collett and R.F. Wendlandt. Formation evaluation of gas hydrate-bearing marine sediments on the blake ridge with downhole geochemical log measurements. In *Proceedings of the Ocean Drilling Program, Scientific Results*, volume 164, pages 199–215, 2000.

[25] F. Heberling, T.P. Trainor, J. Lützenkirchen, P. Eng, M.A. Denecke, and D. Bosbach. Structure and reactivity of the calcite–water interface. *Journal of colloid and interface science*, 354(2):843–857, 2011.

[26] H.D. Schulz and M. Zabel. *Marine geochemistry*. Springer, 2nd edition, 2006.

[27] J.E. Kogel, N.C. Trivedi, J.M. Barker, and S.T. Krukowsk. *Industrial minerals & rocks: commodities, markets, and uses*. SME, 7th edition, 2006.

[28] E.G. Hammerschmidt. Formation of gas hydrates in natural gas transmission lines. *Industrial & Engineering Chemistry*, 26(8):851–855, 1934.

[29] Y.F. Makogon. Hydrates of natural gas. Petroleum Engineering UPSTREAM.

[30] E. D. Sloan Jr. *Clathrate Hydrates of Natural Gases, Revised and Expanded*. CRC Press, 2nd edition, 1998.

[31] J. Carroll. *Natural Gas Hydrates: A Guide for Engineers*. Gulf Professional Publishing, 2nd edition, 2009.

[32] E.D. Sloan Jr. and C. Koh. *Clathrate hydrates of natural gases*. CRC press, 3rd edition, 2007.

[33] *Charting the future of methane hydrate research in the United States*. National Academies Press, 2004.

[34] Y.F. Makogon. Perspectives for the development of gas hydrate deposits. In *Gas hydrates and permafrost: Proceedings of the 4th Canadian Permafrost Conference*, pages 299–304, 1982.

[35] C. Giavarini and K. Hester. *Gas hydrates: immense energy potential and environmental challenges*. Springer Science & Business Media, 2011.

[36] J. Meller et al. Molecular dynamics. *eLS*, 2001.

[37] J.M. HAILE. *Molecular dynamics simulation elementary Methods*. John Wiley & Sons, 1997.

[38] A.R. Leach. *Molecular modelling: principles and applications*. Pearson education, 2nd edition, 2001.

[39] C.R. de Oliveira and T. Werlang. Ergodic hypothesis in classical statistical mechanics. *Revista Brasileira de Ensino de Física*, 29(2):189–201, 2007.

[40] F. Reif. *Fundamentals of statistical and thermal physics*. Waveland Press, 2009.

[41] J.D. Anderson and J. Wendt. *Computational fluid dynamics*, volume 206. Springer, 1995.

[42] D. Frenkel and B. Smit. *Understanding molecular simulation: from algorithms to applications*, volume 1. Academic press, 2nd edition, 2001.

[43] F. Jensen. *Introduction to computational chemistry*. John Wiley & Sons, 2nd edition, 2013.

[44] A. Hinchliffe. *Molecular modelling for beginners*. John Wiley & Sons, 2005.

[45] E.L. Pollock and J. Glosli. Comments on p^3m, fmm, and the ewald method for large periodic coulombic systems. *Computer Physics Communications*, 95(2):93–110, 1996.

[46] R.W. Hockney and J.W. Eastwood. *Computer simulation using particles*. CRC Press, 1988.

[47] S. Nosé. A unified formulation of the constant temperature molecular dynamics methods. *The Journal of chemical physics*, 81(1):511–519, 1984.

[48] W.G. Hoover. Canonical dynamics: equilibrium phase-space distributions. *Physical Review A*, 31(3):1695, 1985.

[49] S. Nosé. A molecular dynamics method for simulations in the canonical ensemble. *Molecular Physics*, 100(1):191–198, 2002.

[50] P.H. Hünenberger. Thermostat algorithms for molecular dynamics simulations. In *Advanced computer simulation*, pages 105–149. Springer, 2005.

[51] H.C. Andersen. Molecular dynamics simulations at constant pressure and/or temperature. *The Journal of chemical physics*, 72(4):2384–2393, 1980.

[52] M. Parrinello and A. Rahman. Polymorphic transitions in single crystals: A new molecular dynamics method. *Journal of Applied physics*, 52(12):7182–7190, 1981.

[53] V. Rühle. Pressure coupling/barostats. *Journal Club Handout*, 2008.

[54] J.-P. Ryckaert, G. Ciccotti, and H.J.C. Berendsen. Numerical integration of the cartesian equations of motion of a system with constraints: molecular dynamics of n-alkanes. *Journal of Computational Physics*, 23(3):327–341, 1977.

[55] G.R. Desiraju and T. Steiner. *The weak hydrogen bond: in structural chemistry and biology*, volume 9. Oxford University Press on Demand, 2001.

[56] T. Giorgino. Computing 1-d atomic densities in macromolecular simulations: the density profile tool for vmd. *Computer Physics Communications*, 185(1):317–322, 2014.

[57] E.M. Chuvilin, E.V. Kozlova, N.A. Makhonina, and V.S. Yakushev. Experimental investigations of gas hydrate and ice formation in methane-saturated sediments. In *Proceeding the 8th International Conference on Permafrost. Zurich, Switzerland*, 2003.

[58] P. Geissbühler, P. Fenter, E. DiMasi, G. Srajer, L.B. Sorensen, and N.C. Sturchio. Three-dimensional structure of the calcite–water interface by surface x-ray scattering. *Surface Science*, 573(2):191–203, 2004.

[59] D. Liu, P. Yuan, H. Liu, T. Li, D. Tan, W. Yuan, and H. He. High-pressure adsorption of methane on montmorillonite, kaolinite and illite. *Applied Clay Science*, 85:25–30, 2013.

[60] L. Ji, T. Zhang, K.L. Milliken, J. Qu, and X. Zhang. Experimental investigation of main controls to methane adsorption in clay-rich rocks. *Applied Geochemistry*, 27(12):2533–2545, 2012.

[61] T. Uchida, S. Takeya, E.M. Chuvilin, R. Ohmura, J. Nagao, V.S. Yakushev, V.A. Istomin, H. Minagawa, T. Ebinuma, and H. Narita. Decomposition of methane hydrates in sand, sandstone, clays, and glass beads. *Journal of Geophysical Research: Solid Earth*, 109(B5), 2004.

[62] W. Neagle and C.H. Rochester. Infrared study of the adsorption of water and ammonia on calcium carbonate. *J. Chem. Soc., Faraday Trans.*, 86(1):181–183, 1990.

[63] D. Tunega, M.H. Gerzabek, and H. Lischka. Ab initio molecular dynamics study of a monomolecular water layer on octahedral and tetrahedral kaolinite surfaces. *The Journal of Physical Chemistry B*, 108(19):5930–5936, 2004.

[64] D. Tunega, G. Haberhauer, M.H. Gerzabek, and H. Lischka. Theoretical study of adsorption sites on the (001) surfaces of 1: 1 clay minerals. *Langmuir*, 18(1):139–147, 2002.

[65] T. Croteau, A.K. Bertram, and G.N. Patey. Adsorption and structure of water on kaolinite surfaces: Possible insight into ice nucleation from grand canonical monte carlo calculations. *The Journal of Physical Chemistry A*, 112(43):10708–10712, 2008.

[66] T. Croteau, A.K. Bertram, and G.N. Patey. Simulation of water adsorption on kaolinite under atmospheric conditions. *The Journal of Physical Chemistry A*, 113(27):7826–7833, 2009.

[67] M.R. Warne, N.L. Allan, and T. Cosgrove. Computer simulation of water molecules at kaolinite and silica surfaces. *Physical Chemistry Chemical Physics*, 2(16):3663–3668, 2000.

[68] Z. Jin and A. Firoozabadi. Effect of water on methane and carbon dioxide sorption in clay minerals by monte carlo simulations. *Fluid Phase Equilibria*, 382:10–20, 2014.

[69] N.H. de Leeuw and S.C. Parker. Atomistic simulation of the effect of molecular adsorption of water on the surface structure and energies of calcite surfaces. *Journal of the Chemical Society, Faraday Transactions*, 93(3):467–475, 1997.

[70] M. Wolthers, D. Di Tommaso, Z. Du, and N.H. de Leeuw. Calcite surface structure and reactivity: molecular dynamics simulations and macroscopic surface modelling of the calcite–water interface. *Physical Chemistry Chemical Physics*, 14(43):15145–15157, 2012.

[71] S. Kerisit, S.C. Parker, and J.H. Harding. Atomistic simulation of the dissociative adsorption of water on calcite surfaces. *The Journal of Physical Chemistry B*, 107(31):7676–7682, 2003.

[72] E. Stöckelmann and R. Hentschke. Adsorption isotherms of water vapor on calcite: A molecular dynamics-monte carlo hybrid simulation using a polarizable water model. *Langmuir*, 15(15):5141–5149, 1999.

[73] S. Fleming and A. Rohl. Gdis: a visualization program for molecular and periodic systems. *Zeitschrift für Kristallographie-Crystalline Materials*, 220(5/6):580–584, 2005.

[74] S.A. Markgraf and R.J. Reeder. High-temperature structure refinements of calcite and magnesite. *American Mineralogist*, 70(5-6):590–600, 1985.

[75] R.D. Goodwin and R. Pyrdz. Densities of compressed liquid methane, and the equation of state. *Journal of Research of the National Bur Stand*, 76(Section A), 1972.

[76] D.L. Bish. Rietveld refinement of the kaolinite structure at 1.5 k. *Clays and Clay Minerals*, 41(6):738–744, 1993.

[77] S. Xiao, S.A. Edwards, and F. Grater. A new transferable forcefield for simulating the mechanics of caco3 crystals. *The Journal of Physical Chemistry C*, 115(41):20067–20075, 2011.

[78] W.L. Jorgensen, J.D. Madura, and C.J. Swenson. Optimized intermolecular potential functions for liquid hydrocarbons. *Journal of the American Chemical Society*, 106(22):6638–6646, 1984.

[79] W.L. Jorgensen, J. Chandrasekhar, J.D. Madura, R W. Impey, and M.L. Klein. Comparison of simple potential functions for simulating liquid water. *The Journal of chemical physics*, 79(2):926–935, 1983.

[80] I.F. Vasconcelos, B.A. Bunker, and R.T. Cygan. Molecular dynamics modeling of ion adsorption to the basal surfaces of kaolinite. *The Journal of Physical Chemistry C*, 111(18):6753–6762, 2007.

[81] W. Humphrey, A. Dalke, and K. Schulten. Vmd: visual molecular dynamics. *Journal of molecular graphics*, 14(1):33–38, 1996.

[82] L. Martínez, R. Andrade, E.G. Birgin, and J.M. Martínez. Packmol: A package for building initial configurations for molecular dynamics simulations. *Journal of computational chemistry*, 30(13):2157–2164, 2009.

[83] S. Plimpton. Fast parallel algorithms for short-range molecular dynamics. *Journal of computational physics*, 117(1):1–19, 1995.

[84] S. Kerisit and S.C. Parker. Free energy of adsorption of water and calcium on the $\{10\bar{1}4\}$ calcite surface. *Chemical communications*, (1):52–53, 2004.

[85] P. Fenter, P. Geissbühler, E. DiMasi, G. Srajer, L.B. Sorensen, and N.C. Sturchio. Surface speciation of calcite observed in situ by high-resolution x-ray reflectivity. *Geochimica et Cosmochimica Acta*, 64(7):1221–1228, 2000.

[86] T.D. Perry, R.T. Cygan, and R. Mitchell. Molecular models of a hydrated calcite mineral surface. *Geochimica et Cosmochimica Acta*, 71(24):5876–5887, 2007.

[87] A. Villegas-Jiménez, A. Mucci, and M.A. Whitehead. Theoretical insights into the hydrated (10.4) calcite surface: Structure, energetics, and bonding relationships. *Langmuir*, 25(12):6813–6824, 2009.

[88] R. Šolc, M.H. Gerzabek, H. Lischka, and D. Tunega. Wettability of kaolinite (001) surfaces—molecular dynamic study. *Geoderma*, 169:47–54, 2011.

[89] J. Wang, A.G. Kalinichev, and R.J. Kirkpatrick. Effects of substrate structure and composition on the structure, dynamics, and energetics of water at mineral surfaces: A molecular dynamics modeling study. *Geochimica et cosmochimica acta*, 70(3):562–582, 2006.

[90] X.L. Hu and A. Michaelides. Water on the hydroxylated (001) surface of kaolinite: From monomer adsorption to a flat 2d wetting layer. *Surface Science*, 602(4):960–974, 2008.

[91] J.D. Smith, C.D. Cappa, K.R. Wilson, B.M. Messer, R.C. Cohen, and R.J. Saykally. Energetics of hydrogen bond network rearrangements in liquid water. *Science*, 306(5697):851–853, 2004.

Appendix I

Atomic density of oxygen and hydrogen atoms of water on mineral surfaces (only distance of 5Å from the surfaces is considered) are shown in the following figures:

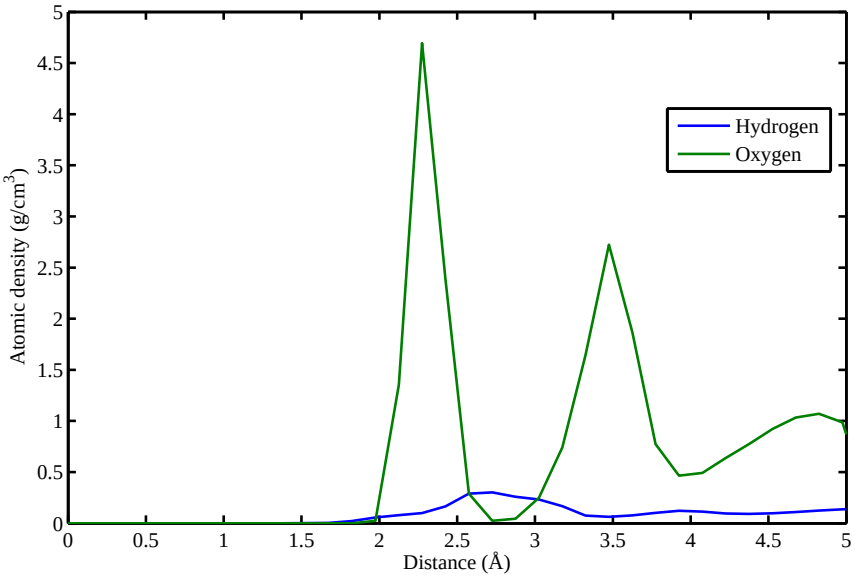

Figure A.1: Atomic densities of hydrogen and oxygen atoms of water on the calcite surface.

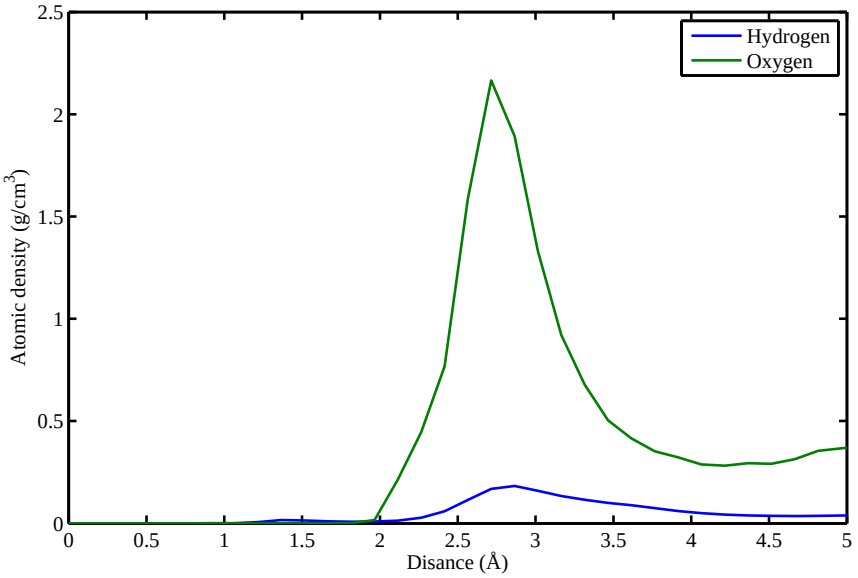

Figure A.2: Atomic density of hydrogen and oxygen atoms of water on the octahedral surface.

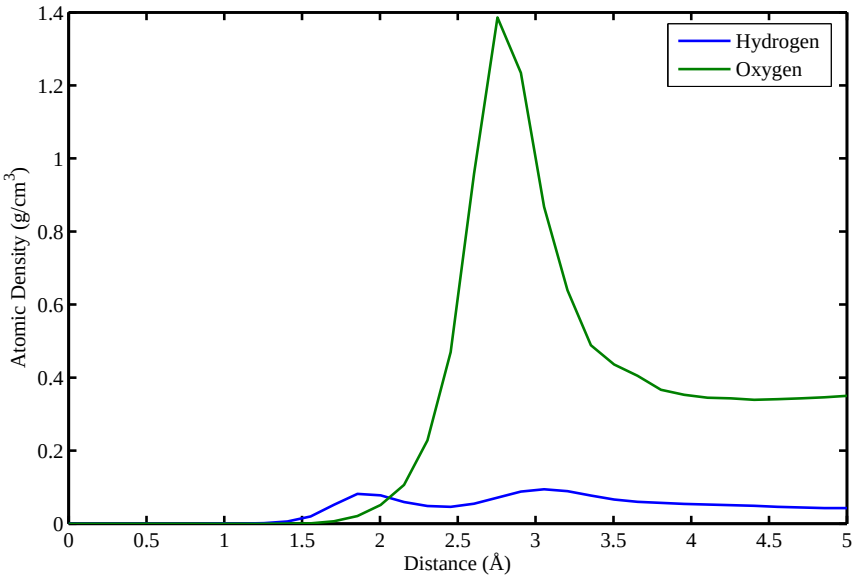

Figure A.3: Atomic density of hydrogen and oxygen atoms of water on the tetrahedral surface.